



Dynamic Wellbore Stability Analysis Under Tripping Operations

Meng Meng¹ · Zahra Zamanipour¹ · Stefan Miska¹ · Mengjiao Yu¹ · E. M. Ozbayoglu¹

Received: 20 May 2018 / Accepted: 31 January 2019 / Published online: 26 February 2019
 © Springer-Verlag GmbH Austria, part of Springer Nature 2019

Abstract

The loadings which act on the wellbore are more frequently dynamic than static, such as the surge/swab pressure caused by tripping operations. The changing rate of loading could induce a change in wellbore stress and result in wellbore instability. The conventional Kirsch solution to calculate wellbore stress is only applicable to the steady state without considering the coupled deformation–diffusion effect. To account for these deficiencies, this paper introduces a coupled poroelastodynamics model to obtain wellbore stress distribution under dynamic loading. The model is solved by the implicit finite-difference method with the surge/swab pressure caused by tripping operations taken as the specific dynamic loading source. Then, failure criteria are applied to analyze dynamic wellbore stability and the hemisphere plots of minimum mud density (MMD) to avoid wellbore collapse are generated. The effect of in-situ stress regimes, failure criteria, and permeable properties on the instability of the borehole has been investigated, and the applicability and accuracy of the conventional failure criteria for dynamic loading conditions have been studied by the extensive triaxial compression tests performed on Bedford limestone under different strain rates. Furthermore, two specific cases have been analyzed and results show that compared with the poroelastodynamics model, the conventional method either overestimates or underestimates the MMD, the difference of which can be as significant as 0.11 g/cm^3 . Not limited to the tripping operations, the developed poroelastodynamics model can be applied to any specific dynamic loading conditions with the fluid inertia neglected.

Keywords Wellbore stability · Tripping · Poroelastodynamics model · Minimum mud density

Abbreviations

MMD	Minimum mud density
MMD _{3DHoek–Bown}	Minimum mud density by 3D Hoek–Bown
MMD _{Mogi–Coulomb}	Minimum mud density by Mogi–Coulomb
MMD _{Modified Lade}	Minimum mud density by Modified Lade
NF	Normal fault
NF-SS	The transition between normal fault and strike-slip
SS	Strike-slip
SS-TF	The transition of the strike-slip and thrust fault
TF	Thrust fault
N30°E	The degree of 30° from North to East

List of Symbols

B	Junction point
B_a, B_b	Upper and lower surface of the junction point B
A_a	Upper surface of the point A
C_b	Lower surface of the point C
Q	Flow rate
Q_{B_a}, Q_{B_b}	Flow rate at B_a, B_b
Q_{t,B_a}, Q_{t,B_b}	Flow rate at position B_b and B_b at time t
Q_{t-1,A_a}, Q_{t-1,C_b}	Flow rate at position A_a and C_b at time $t - 1$
t	Time
p	Pressure
p_{t,B_b}, p_{t,B_a}	Pressure of position B_b and B_a at time t
p_{t-1,A_a}, p_{t-1,C_b}	Pressure of position A_a and C_b at time $t - 1$
p_s	Surface pressure
S_{AB}, S_{BC}	Characteristic impedances of sections AB and BC
ΔA_B	The change of pipe cross-sectional area at junction B

✉ Meng Meng
 mem282@utulsa.edu

¹ Department of Petroleum Engineering, The University of Tulsa, McDougall School of Petroleum Engineering, North Campus 211D, Tulsa, OK, USA

V_t	Pipe velocity at time t
Δp	The loss of pressure in the artificial orifice
$\sigma_{ij,j}$	Stress gradient tensor
σ_{ij}	Stress tensor
$\sigma_r, \sigma_\theta, \sigma_z$	Radial, tangential and vertical normal stress
$\sigma_{r\theta}, \sigma_{\theta z}, \sigma_{rz}$	Shear stress terms
u_i	Displacement vector
u_r, u_θ, u_z	Radial, tangential and vertical normal displacement
ε_{ij}	Strain tensor
$\varepsilon_r, \varepsilon_\theta, \varepsilon_z$	Radial, tangential and vertical normal strain
ε_{kk}	Volumetric strain
r, θ, z	Radial, tangential and vertical coordinate
δ_{ij}	Kronecker delta
ρ	Density
G, λ	Lame parameters
ν	Poisson's ratio
α	Biot coefficient
S_z	Specific storage at constant strain
Q_{fs}	Explicit fluid sources
k	Permeability
μ	Fluid viscosity
K_u	Undrained bulk modulus
K	Drained bulk modulus
c_v	Hydraulic diffusivity
$\sigma_r^1, \sigma_\theta^1, \sigma_z^1$	Stress solution of Eq. (12)
$\sigma_r^2, \sigma_\theta^2, \sigma_z^2$	Far-field stress terms
σ_v	Vertical stress
σ_H	Maximum horizontal stress
σ_h	Minimum horizontal stress
θ	Wellbore circumferential angle
r_w	Wellbore radius
$\sigma_x^0, \sigma_y^0, \sigma_z^0, \sigma_{xy}, \sigma_{xz}, \sigma_{yz}$	In-situ stress terms in the Cartesian coordinate
Diff_{ave}	Non-dimensional average prediction difference
Diff_{abs}	Non-dimensional absolute prediction difference
$[(\sigma'_1)_{\text{pre}}]_i$	Predicted major principal stress at failure
$[(\sigma'_1)_{\text{exp}}]_i$	Experimental major principal stress at failure
UCS	Uni-axial rock strength
n	The total number of data points
ξ	Non-dimensional distance
τ	Non-dimensional time
ϕ	Non-dimensional displacement
S_r	Non-dimensional radial stress
χ	Non-dimensional pore pressure

c	Compression wave velocity
p_0	Static wellbore pressure
\varnothing	Porosity

1 Introduction

Wellbore instability has been a long-term issue in the drilling industry. It increases non-productive time, causing billions of dollars to be lost every year. In the past decades, researchers have studied wellbore stability with aspects to consolidation effect, temperature effect, chemical effect, etc. No matter which kind of effects that need to be studied, accurate wellbore stress distribution is the prerequisite for wellbore stability analysis. Nearly, all the innovative theoretical methods have to be utilized through the changes of stress distribution using the superposition principle. In 1898, the Kirsch solution was published to calculate stress distribution around a circular hole in an infinite plate. Later, Bradley (1979) showed the elastic analytical solution of stresses around the wellbore by taking advantage of the Kirsch solution together with the solution by Fairhurst (1967). It was then regarded as the general solution to calculate stress distribution by many researchers (Aadnoy 1987; Fjar et al. 2008; Chen 2008; Jaeger et al. 2009; Zoback 2010; Meng 2019b). Although this method is commonly used by most researchers, one important point to be noted is this method is mostly used for the steady state. It is different from the solution strategy provided by Detournay and Cheng (1988), which was used for wellbore stress distribution under instantaneous drilling or wellbore excavation. They decomposed the calculation of wellbore stresses into three modes including far-field isotropic stress, virgin pore pressure, and a far-field stress deviator. The far-field stress deviator could cause induced pore pressure. The solution is more complex than the general Kirsch solution and requires the Laplace transform and numerical Laplace inverse methods to get the final results.

The tripping operation is one important procedure in the drilling process due to the necessities of changing the drill bit, downhole assembly, subsea equipment, etc. During tripping operations, the drill string movement generates a dynamic force resulting in a longitudinal wave. The wave propagates along the drill string and causes a variance in the wellbore pressure. The reduced pressure caused by tripping the drill string outside the wellbore is called swab pressure and the increased pressure caused by tripping the drill string inside the wellbore is called surge pressure. The surge/swab pressure is one major reason for severe drilling problems, including wellbore instability, lost circulation, fluid kick, or even blowouts (Cannon 1934; Lubinski 1977; Mitchell 1988). Tripping velocity is commonly regarded as one major factor that is positively related to the values

of surge/swab pressure. If the tripping velocity is slow, the surge/swab pressure is low enough to guarantee safe drilling process. However, a slow tripping velocity makes drilling very time consuming, and the daily well drilling cost is extremely high, especially in the offshore drilling. If the tripping velocity is high, safety issues, especially wellbore instability, will occur. Therefore, it is highly necessary to analyze the wellbore stability under tripping operation. To realize this goal, there are three major steps: the prediction of surge/swab pressure, the calculation of dynamic stress, and the application of failure criteria.

The prediction of surge/swab pressure has gained the interest of drilling engineers for a long time (Crespo 2012; Mme 2012; Wang 2013; Karlsen 2014). Cannon (1934) first proposed that the swab pressure could cause fluid influx, lost circulation, or even blowouts. Then, it was realized that the prediction of the surge/swab pressure is significant. Early researchers (Burkhardt 1961; Schuh 1964; Fontenot 1974) used “steady flow” models to predict surge/swab pressure. The results were not realistic, because it neglected fluid inertia and compressibility of the fluid and wellbore. Later, Lubinski (1977) initially proposed one fully dynamic surge-pressure model used for Bingham plastic fluids. This model was based on transient wave propagation theory which considered fluid compressibility and wellbore expansion. Mitchell (1988) further improved the dynamic model by coupling pipe and annulus pressures through pipe elasticity. Based on the former studies, Zamanipour (2015, 2016) developed the program to predict dynamic surge/swab pressure for both Bingham plastic fluids and power-law fluids.

Although the conventional Kirsch method and Detournay and Cheng’s method are the widely used methods, neither of them is appropriate for dynamic stress distribution of the wellbore under tripping operations. The Kirsch method is used for steady state, but dynamic surge/swab is transient. Detournay and Cheng’s method is used for excavation, but tripping operations occur after the wellbore has already been excavated. Therefore, new methods should be proposed to calculate dynamic stress around the wellbore under tripping operations. Zamanipour (2016) studied stress distribution around a directional wellbore under tripping conditions. It took advantage of the method proposed by Wang (2000) which regarded the surge/swab pressure effect as the sudden pressurization of a borehole. This method neglected the inertia effect in the equilibrium equation, which is one significant difference between dynamic and static loading. Zhang et al. (2016) used the instantaneous drilling method to study transient stress distribution around the wellbore. Detournay and Cheng’s method is usually used for wellbore excavation, or instantaneously drilling process, but tripping operations occur right after the wellbore has already been drilled. The influence of deviatoric loading on the tangential stress only dissipates slowly when the formation permeability is very

low. Therefore, a new method should be proposed to calculate dynamic stress distribution under tripping operations.

The last step of wellbore stability analysis is the application of failure criteria. During tripping operations, both shear failure and tensile failure may happen. Shear failure, also called wellbore collapse, could happen during tripping out. Tensile failure, also called wellbore fracturing, could happen during tripping in. For the wellbore collapse, there are many failure criteria, including Mohr–Coulomb failure criterion, Mogi–Coulomb failure criterion (Al-Ajmi 2006; Islam et al. 2010), Modified Lade failure criterion (Ewy 1999), Hoek–Brown failure criterion, 3D Hoek–Brown failure criterion (Zhang 2007, 2008), and Drucker–Prager failure criterion. For wellbore fracturing, the pressurization rate is important, because it can influence the breakdown pressure of a wellbore. Overall, a reasonable failure criterion should be used for analyzing wellbore stability under dynamic loading conditions (Zhao 2000; Zhou and Zhao 2011) and shear failure is usually focused when researchers work on wellbore stability analysis (Zoback 2010). To the best of our knowledge, whether the static failure criteria could be used for wellbore stability analysis under tripping operations and which is the best option has not been studied by past researchers.

In this paper, a new poroelastodynamics model is established to calculate dynamic stress distribution under tripping operations. It is solved numerically by the implicit finite-difference method. The dynamic surge/swab pressure is predicted based on Lubinski’s method. They are implemented into the numerical solving procedure of the poroelastodynamics model to calculate dynamic stress distribution. Then, different failure criteria are applied to the dynamic wellbore collapse analysis under tripping operations. Furthermore, the triaxial compression test has been performed on Bedford limestone under different confining pressure and strain rate. The results are used to check the accuracy of different failure criteria and verify they can be used for wellbore stability analysis under tripping operations.

2 Modeling and Solution Strategy

2.1 Prediction of Dynamic Surge/Swab Pressure

The prediction of surge/swab pressure is calculated using Lubinski’s method (1977, 1988) and the procedures are introduced clearly by Zamanipour (2015, 2016) and Zhang et al. (2016, 2018). Only the basic procedures will be introduced here. To calculate the surge/swab pressure, the wellbore needs to be divided by a discrete number of small sections. The connection between two adjacent small sections is called “junctions with artificial orifices” by Lubinski, which is shown in Fig. 1. Mechanisms of energy dissipation

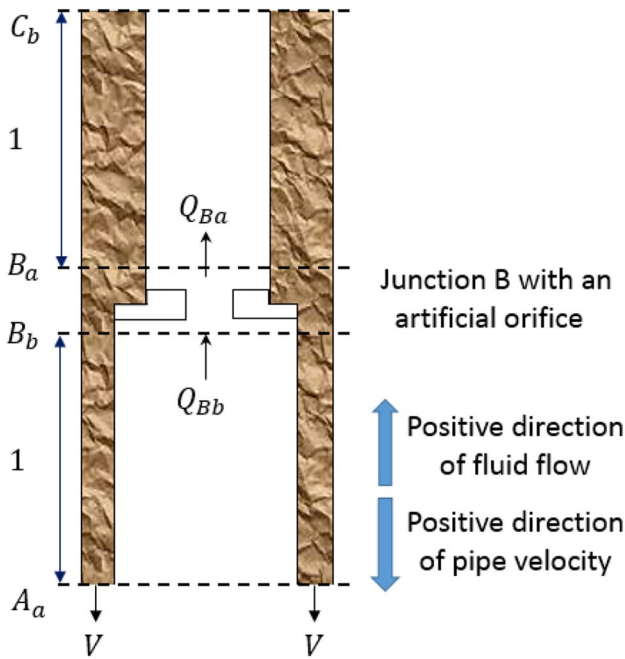


Fig. 1 Schematic diagram of junction with an artificial orifice

(irreversible drops of pressure) are concentrated at these junctions.

Consider that at time $t - 1$, flow rates Q and pressure p are known at the junctions, and it is now desired to calculate Q and p at time t at junction B . The following two equations of propagation are the algebraic equivalents of the corresponding Bergeron graphical construction:

$$p_{t,Bb} - p_{t-1,Aa} = -S_{AB}(Q_{t,Bb} - Q_{t-1,Aa}), \tag{1}$$

$$p_{t,Ba} - p_{t-1,Cb} = +S_{BC}(Q_{t,Ba} - Q_{t-1,Cb}), \tag{2}$$

in which the first subscript pertains to time and the second to location. S_{AB} and S_{BC} are characteristic impedances of sections AB and BC , respectively. $p_{t,Bb}$ and $p_{t,Ba}$ are pressure of position B_b and B_a at time t . $p_{t-1,Aa}$ and $p_{t-1,Cb}$ are pressure of position A_a and C_b at time $t - 1$, respectively. $Q_{t,Bb}$ and $Q_{t,Ba}$ are flow rate of position B_b and B_a at time t . $p_{t-1,Aa}$ and $p_{t-1,Cb}$ are flow rate of position A_a and C_b at time $t - 1$, respectively. Upward flow is considered positive, which dictates the signs of S_{AB} and S_{BC} .

In Eqs. (1) and (2), there are four unknowns at time t at the junction B , namely: $p_{t,Bb}$, $p_{t,Ba}$, $Q_{t,Bb}$, $Q_{t,Ba}$. Therefore, we need two more equations to find these unknown values. These equations will pertain to changes in values of Q and p between B_b and B_a .

Assume the downward as the positive direction of pipe velocity, the continuity equation is

$$Q_{t,Ba} - Q_{t,Bb} = V_i \Delta A_B, \tag{3}$$

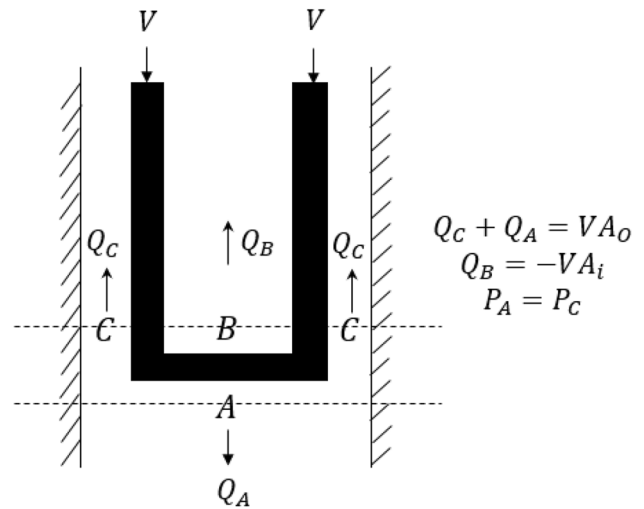


Fig. 2 Continuity and pressure loss equations at the lower end of the pipe string

in which ΔA_B is the change in pipe cross-sectional area at the junction B , and V_i is pipe velocity at time t .

The continuity equation applies to all junctions except at the surface, at the bottom of the hole, and at the lower end of the pipe string. There is no continuity equation at the surface. At the bottom of the hole, $Q = 0$. The continuity equation at the lower end of the pipe string is written in Fig. 2. If there is no cross-sectional area change, then $Q_{t,Ba} = Q_{t,Bb}$.

The fourth equation is

$$p_{t,Ba} - p_{t,Bb} = \Delta p, \tag{4}$$

in which Δp is the loss of pressure in the artificial orifice.

For the pressure boundary condition, the pressure loss Eq. (4) applies to all junctions except at the surface and at the lower end of the pipe string. At the surface, $p_s = 0$. At the lower end of the pipe string, the boundary conditions are shown in Fig. 2.

2.2 Dynamic Stress Distribution

2.2.1 Governing Equations

To obtain the governing equations for stress distribution around the wellbore under dynamic loading, fundamental knowledge of poroelasticity should be used. The normal method is to combine strain–displacement relation, equations of motion in poroelastic medium, and Hooke’s law together. Then, the governing equations for the poroelastodynamics model could be generated. The major assumptions are: (1) the rock is continuous and isotropic; (2) the plane strain condition works for this problem; (3) the fluid inertia can be neglected; and (4) it is a cylindrically symmetrical displacement field.

For cylindrical coordinates, the equilibrium equations are (Sadd 2009)

$$\sigma_{ij,j} = \rho \frac{\partial^2 u_i}{\partial t^2}, \tag{5}$$

where $\sigma_{ij,j}$ is the stress gradient tensor, ρ is density, u_i is the displacement vector.

The constitutive equations are

$$\sigma_{ij} = 2G\sigma_{ij} + 2G \frac{\nu}{1-2\nu} \epsilon_{kk} \delta_{ij} - \alpha p \delta_{ij} \rho \frac{\partial^2 u_i}{\partial t^2}, \tag{6}$$

where σ_{ij} is the stress tensor, G is Lamé parameter, ν is Poisson’s ratio, ϵ_{kk} is the volumetric strain, δ_{ij} is the Kronecker delta, and α is the Biot coefficient.

The strain–displacement relation is

$$\epsilon_r = \frac{\partial u_r}{\partial r}, \epsilon_\theta = \frac{1}{r} \left(u_r + \frac{\partial u_\theta}{\partial \theta} \right), \epsilon_z = \frac{\partial u_z}{\partial z}, \tag{7}$$

where ϵ_r , ϵ_θ , and ϵ_z are the radial, tangential, and vertical normal strain, respectively. r , θ , and z are radial, tangential, and vertical coordinates, respectively.

Through combining Eqs. (5) to (7), the governing equation for poroelastodynamics becomes

$$(2G + \lambda) \left(\frac{\partial^2 u_r}{\partial r^2} + \frac{1}{r} \frac{\partial u_r}{\partial r} - \frac{u_r}{r^2} \right) - \frac{\alpha}{G} \frac{\partial p}{\partial r} = \rho \frac{\partial^2 u_r}{\partial t^2}, \tag{8}$$

where λ is Lamé parameter.

For the constitutive equations, either pore pressure or the increment of fluid content can be chosen as the fluid variable. A nonhomogeneous diffusion equation for pore pressure is

$$\alpha \frac{\partial \epsilon_{kk}}{\partial t} + S_\epsilon \frac{\partial p}{\partial t} = \frac{k}{\mu} \nabla^2 p + Q_{fs}, \tag{9}$$

where S_ϵ is the specific storage at constant strain, k is permeability, and μ is fluid viscosity:

$$S_\epsilon = \frac{\alpha^2}{K_u - K}, \tag{10}$$

where α is the Biot’s coefficient, K_u is the undrained bulk modulus, and K is the drained bulk modulus.

For Eq. (9), the pore pressure field is coupled with the time rate of change of the volumetric strain. This equation can be mathematically uncoupled from the mechanical equilibrium equations for an irrotational displacement field in an infinite domain without body forces (Wang 2000):

$$\nabla^2 p = \frac{1}{c_v} \frac{\partial p}{\partial t}, \tag{11}$$

where c_v is the hydraulic diffusivity.

Assuming cylindrically symmetrical displacement field and no shear stresses acting upon the element, then the normal stresses σ_r and tangential stress σ_θ are independent of the tangential coordinate θ . Also assuming plane strain and neglecting in-situ stress, the governing equation could be achieved by combining Eqs. (5) to (11):

$$\begin{cases} (2G + \lambda) \left(\frac{\partial^2 u_r}{\partial r^2} + \frac{1}{r} \frac{\partial u_r}{\partial r} - \frac{u_r}{r^2} \right) - \frac{\alpha}{G} \frac{\partial p}{\partial r} = \rho \frac{\partial^2 u_r}{\partial t^2} \\ \frac{\partial^2 p}{\partial r^2} + \frac{1}{r} \frac{\partial p}{\partial r} = \frac{1}{c_v} \frac{\partial p}{\partial t}, \end{cases} \tag{12}$$

The solving strategy of Eq. (12) is explained in detail in "Appendix A1". In this model, the fluid inertia term is neglected. This is called up formulation by Zienkiewicz (1980), Schanz (2009), and Wrana (2013). This approximation is economical and convenient in the transient numerical analysis, and it will not influence the result when the loading frequency is low. For the influence of surge/swab pressure, neglecting fluid inertia is reasonable, since the loading frequency is low. Furthermore, even if we have a significantly high loading frequency inside the wellbore, fluid inertia could also be neglected when the rock is relatively impermeable, such as shale rock, or the wellbore surface is sealed by mud cake.

2.2.2 Wellbore Stress Distribution

To get the total wellbore stress distribution, reasonable boundary conditions should be used. For the diffusion equation in Eq. (12), the internal boundary is wellbore pressure plus dynamic surge/swab pressure, and the external boundary is the formation pressure. For the displacement equation, the internal boundary is wellbore pressure plus dynamic surge/swab pressure, the external boundary is zero rather than far-field stress. Taking advantage of the superposition principle, the total stress is the stress calculated by Eq. (12) plus the far-field stress. Here, the maximum horizontal stress is assumed to exist and is not the same as the minimum horizontal stress:

$$\sigma_r = \sigma_r^1 + \sigma_r^2, \sigma_\theta = \sigma_\theta^1 + \sigma_\theta^2, \sigma_z = \sigma_z^1 + \sigma_z^2, \tag{13}$$

where σ_r^1 , σ_θ^1 , and σ_z^1 are the solution of Eq. (12), and σ_r^2 , σ_θ^2 , and σ_z^2 are the far-field stress terms for radial, tangential, and vertical stresses. The far-field stress terms are

$$\sigma_r^2 = \left(\frac{\sigma_x^0 + \sigma_y^0}{2}\right)\left(1 - \frac{r_w^2}{r^2}\right) + \left(\frac{\sigma_x^0 - \sigma_y^0}{2}\right)\left(1 + \frac{3r_w^4}{r^4} - \frac{4r_w^2}{r^2}\right)\cos 2\theta + \sigma_{xy}\left(1 + \frac{3r_w^4}{r^4} - \frac{4r_w^2}{r^2}\right)\sin 2\theta$$

$$\sigma_\theta^2 = \left(\frac{\sigma_x^0 + \sigma_y^0}{2}\right)\left(1 + \frac{r_w^2}{r^2}\right) - \left(\frac{\sigma_x^0 - \sigma_y^0}{2}\right)\left(1 + \frac{3r_w^4}{r^4}\right)\cos 2\theta - \sigma_{xy}\left(1 + \frac{3r_w^4}{r^4}\right)\sin 2\theta, \tag{14}$$

$$\sigma_z^2 = \sigma_z^0 - \nu \left[\frac{2r_w^2}{r^2}(\sigma_H - \sigma_h)\cos 2\theta + 4\sigma_{xy}\frac{r_w^2}{r^2}\sin 2\theta \right],$$

where σ_H and σ_h are maximum and minimum horizontal stresses, respectively. $\sigma_x^0, \sigma_y^0, \sigma_z^0, \sigma_{xy}, \sigma_{xz},$ and σ_{yz} are in-situ stress terms in the Cartesian coordinate. θ is the circumferential angle. r_w is the wellbore radius.

Here, the detailed derivation of Eq. (14) is shown in the "Appendix A2". The conventional Kirsch solution provided by Chen (2008) considering seepage effect is also shown in the "Appendix A2".

2.3 Failure Criteria

Within the last decades, a number of failure criteria have been proposed. Many of them could be used to describe rock failure under static and quasi-static loading conditions. Under dynamic and cyclic loading, the rock failure is controlled by different parameters and relations. However, there is no agreement on the divisions for static, quasi-static, and dynamic loading conditions. According to several articles (Cai et al. 2007; Liang 2015), when the strain rate is lower than $5 \times 10^{-4}/s$, it is static loading. When the strain rate is between $5 \times 10^{-4}/s$ and $1 \times 10^2/s$, it is quasi-static or quasi-dynamic loading. When the strain rate is larger than $1 \times 10^2/s$, it is dynamic loading. The divisions of strain rate with respect to engineering activities are shown in Fig. 3. The magnitude of the strain rate of the wellbore caused by tripping operations is less than $10^{-3}/s$ and mostly less than $10^{-4}/s$, which lies in the static loading domain. Therefore, the commonly used failure criteria of rock could be studied and selected to describe wellbore stability during tripping

operations. This will also be confirmed by the triaxial compression test which is described in Sect. 3.

Failure of rocks can be described by stress criteria, energy criteria or strain criteria. Stress criteria are the most popular one in rock mechanics. Some criteria only consider the minimum principal stress σ_3 and the maximum principal stress σ_1 , such as Mohr–Coulomb, Hoek–Brown, and Drucker–Prager failure criteria. However, much evidence has shown that the intermediate principal stress does indeed influence rock strength (Handin et al. 1967; Fjær 2002; Al-Ajmi 2006). Then, more advanced criteria were proposed and they include the influence of intermediate principal stress σ_2 , such as Mogi–Coulomb criterion, Modified Lade criterion, and 3-D Hoek–Brown criterion. Finally, six failure criteria have been applied to analyze wellbore stability under tripping operations. The detailed explanations of these six failure criteria have been introduced by many researchers (Fjar et al. 2008; Zoback 2010; Ulusay 2014), so it will not be repeated in this paper.

2.4 Calculation flow chart

A flowchart shown in Fig. 4 has been made to present the logical sequence to analyze dynamic wellbore stability under tripping conditions.

3 Experiments

The tested rock is Bedford limestone located in northeast Oklahoma, US. Standard cylindrical specimens of 50 mm in diameter and 100 mm in length are drilled from the same

Strain rate	...	10^{-6}	10^{-5}	10^{-4}	10^{-3}	10^{-2}	10^{-1}	10^0	10^1	10^2	10^3	10^4	...
Divided by mining domain		Low strain rate		Medium strain rate						High strain rate			
		Static loading		Quasi-static	Quasi-dynamic			Dynamic loading					
Oilfield activity		Tripping			Seismic waves caused by earthquake						Perforation		

Fig. 3 Divisions of strain rate with respect to engineering activities

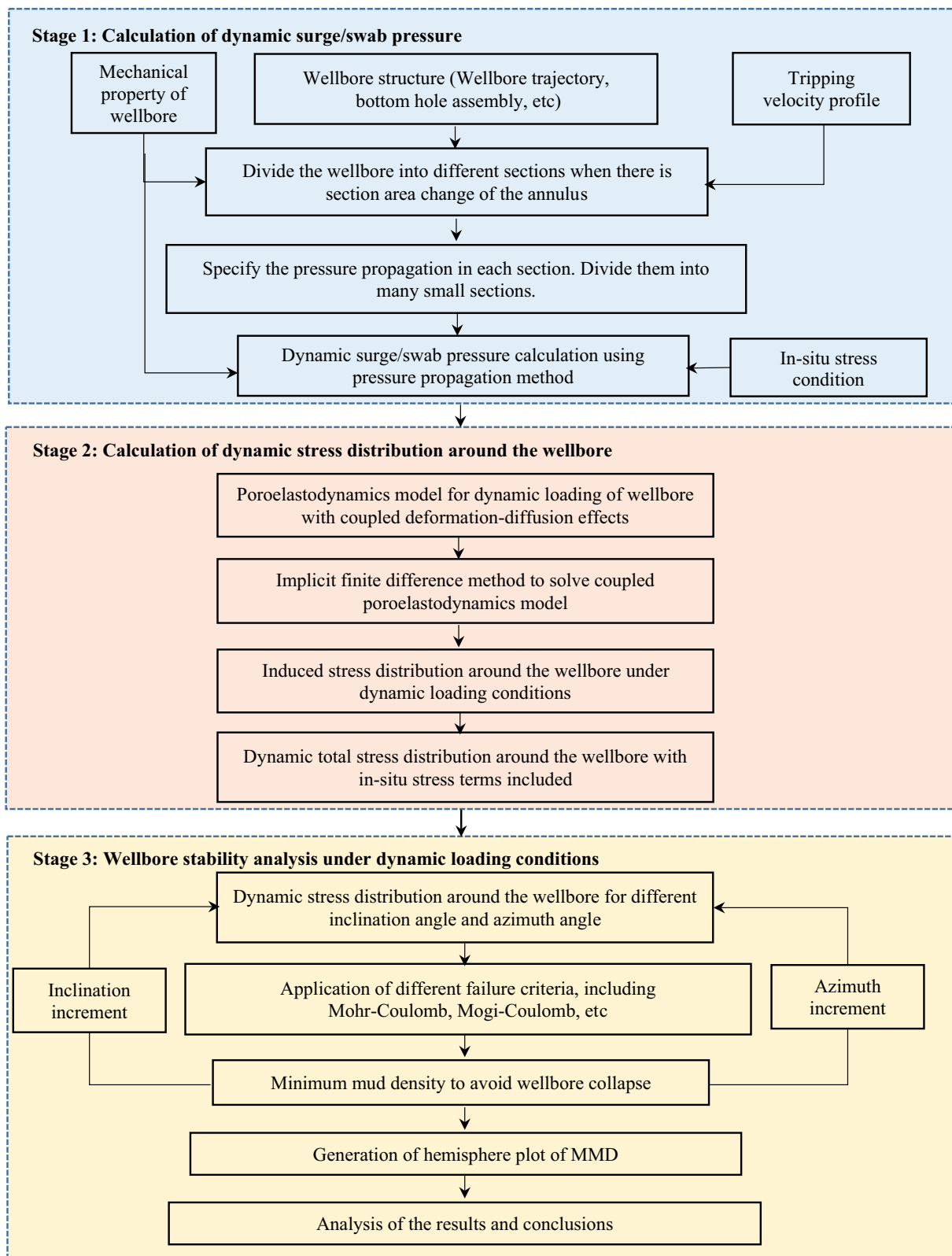


Fig. 4 Flowchart for analyzing wellbore stability under tripping operations

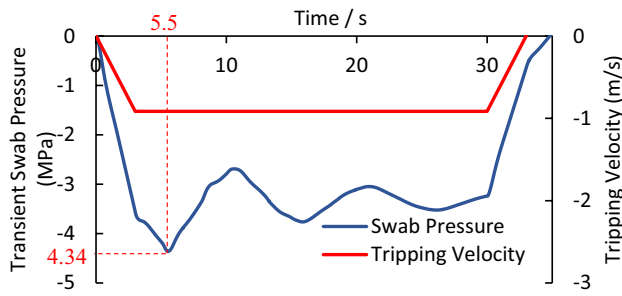


Fig. 5 Tripping velocity, dynamic surge/swab pressure versus time

block. The sample preparation and triaxial compression test are performed based on ASTM standards.

The GCTS electric hydraulic servo-controlled rock mechanics facility was used for the triaxial compression test of limestone under different confining pressures and strain rates. The confining pressure is 0, 6.9 MPa, 13.8 MPa, and 20.7 MPa. The strain rate of the monotonic loading is $1 \times 10^{-6}/s$, $1 \times 10^{-5}/s$, and $1 \times 10^{-4}/s$. The purpose of experimental work is to check whether well-known static failure criteria could be used for wellbore stability analysis under dynamic tripping operations. The basic procedures are: (1) using the data of different confining pressures with the slowest strain rate of $1 \times 10^{-6}/s$ to generate static rock cohesion and internal angle; (2) plot constitutive failure line for different failure criteria; and (3) check the accuracy of different failure criteria by comparing experimental data of higher strain rate with the constitutive failure line. All the results are presented in Sect. 4.4.

4 Results and Discussion

4.1 Dynamic Surge/Swab Pressure

Figure 5 presents the tripping velocity profile and transient swab pressure profile during tripping out. They are calculated using the parameters, as listed in Table 1. The velocity is negative, because the downward movement of drill pipe is assumed to be positive. The pressure is negative, because the swab pressure reduces the wellbore pressure. It shows that the swab pressure is transient, and at about 5.5 s, the absolute transient swab pressure is at a maximum, which is 4.34 MPa. The wellbore stress will be calculated at this moment. If the wellbore collapse can be avoided at this point, other moments are also considered to be safe.

4.2 Distribution of Dynamic Wellbore Stress

To calculate the distribution of dynamic wellbore stress, the wellbore azimuth angle is assumed to be zero, which also means that the maximum horizontal stress direction is north/south. The wellbore inclination angle is also assumed to be zero. Using the inputs listed in Table 2, the wellbore stress calculated by the conventional method and the poroelastodynamics method will be compared.

The comparison of stress distribution between the conventional model and the poroelastodynamics model is shown in Fig. 6. In each of these four figures, the maximum horizontal stress is in the $N30^\circ E$ direction, and the minimum horizontal stress is in the $N60^\circ W$ direction. The degree 0,

Table 1 Input parameters for calculation in case I

Parameter	Value	Unit	Parameter	Value	Unit
Wellbore			Formation		
Hole diameter	0.2286	m	Formation pressure	29.4	MPa
Wellbore length	3000	m	Cohesion	25	MPa
Drill pipe length	2771.4	m	Internal angle	20	°
Drill pipe OD	0.127	m	Biot coefficient	0.8	–
Drill pipe ID	0.1016	m	Drilling fluid		
Drill collar length	164.592	m	Drilling fluid type	Bingham	
Drill collar OD	0.2032	m	Drilling fluid density	1222	kg/m ³
Drill collar ID	0.127	m	Plastic viscosity	0.045	Pa.s
Surface casing length	2542.8	m	Yield value	7.18	Pa
Surface casing OD	0.25654	m			
Surface casing ID	0.23622	m			

Table 2 Input parameters for calculation

Depth/m	$\sigma_v/(g/cm^3)$	$\sigma_H/(g/cm^3)$	$\sigma_H/(g/cm^3)$	Pore pressure $P/(g/cm^3)$	$\alpha/(^\circ)$	$i/(^\circ)$
3000	2.61	2.31	1.85	1.01	N30°E	0

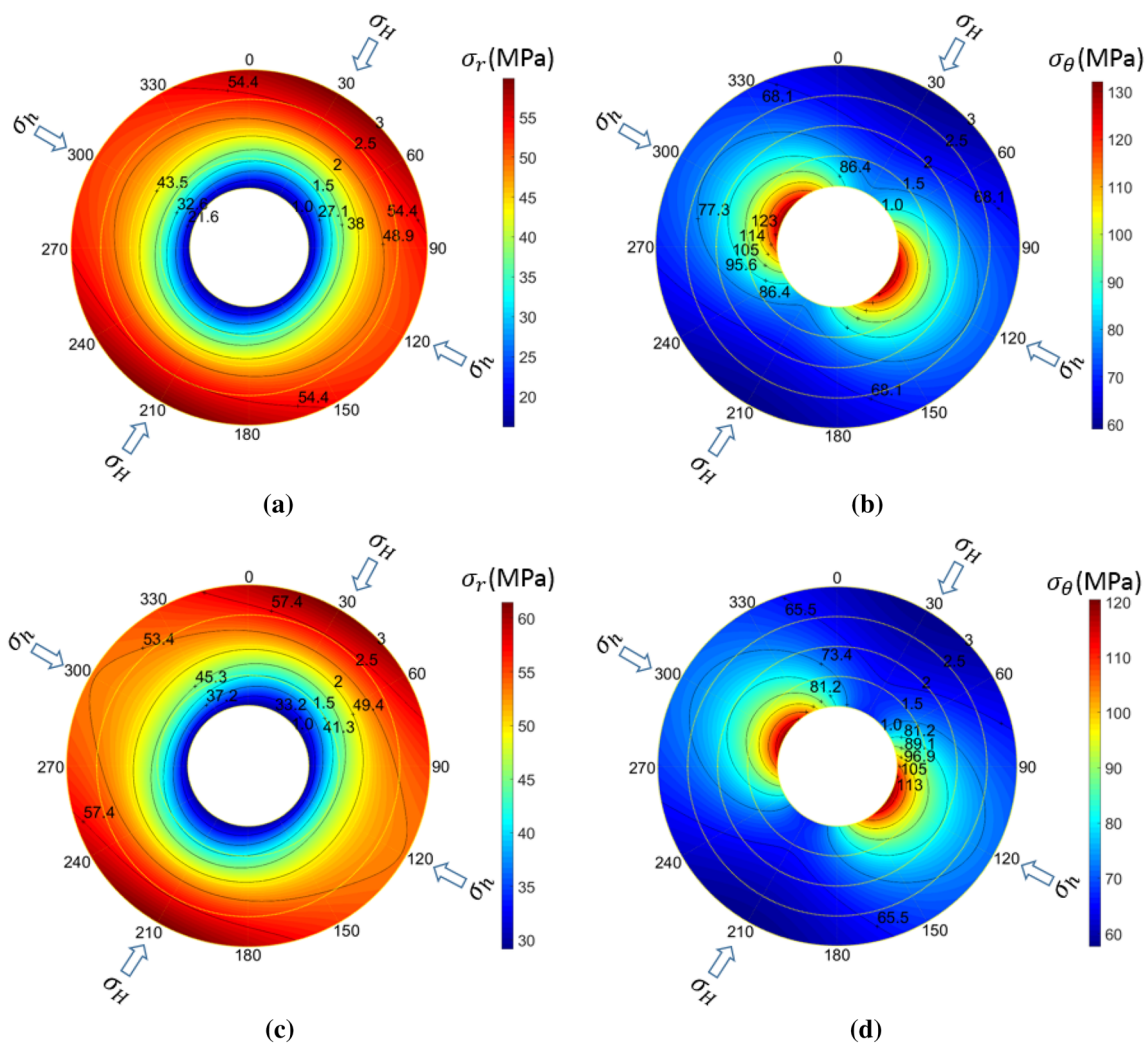


Fig. 6 Wellbore stress distribution under tripping out condition, **a** is radial stress calculated by the conventional method; **b** is tangential stress calculated by the conventional method; **c** is radial stress calcu-

lated by the poroelastodynamics model; **d** is tangential stress calculated by the poroelastodynamics model

30,... 330 represents the circumferential angle of the wellbore. The yellow dotted circles with a different radius of 1, 1.5, 2, 2.5, and 3 represent dimensionless distance $\xi(r/r_w)$. In the color bar, the unit of the number is MPa. Figure 6a, b shows, respectively, the radial stress, tangential stress calculated by the conventional method. Figure 6c, d shows, respectively, the radial stress and tangential stress calculated by the poroelastodynamics model. From these figures, it is found that radial stress increases with the radial distance, while tangential stress decreases with radial distance. Both radial stress and tangential stress are influenced by the circumferential angle due to the influence of non-uniform hydrostatic stress. After comparing Fig. 6a–d, it is found that the conventional Kirsch solution is distinguishable from the poroelastodynamics solution. For the conventional Kirsch solution, the radial stress is between 30 and 61 MPa and the

Table 3 Parameters of in-situ stress

Cases	Stress regime	$\sigma_v(\text{g/cm}^3)$	$\sigma_H(\text{g/cm}^3)$	$\sigma_h(\text{g/cm}^3)$	Pore pressure $P(\text{g/cm}^3)$
1	Normal fault (NF)	2.61	2.31	1.85	1.01
2	NF-SS	2.49	2.49	1.73	1.01
3	Strike-slip (SS)	2.08	2.31	1.73	1.01
4	SS-TF	2.08	2.54	2.08	1.01
5	Thrust fault (TF)	2.08	2.54	2.19	1.01

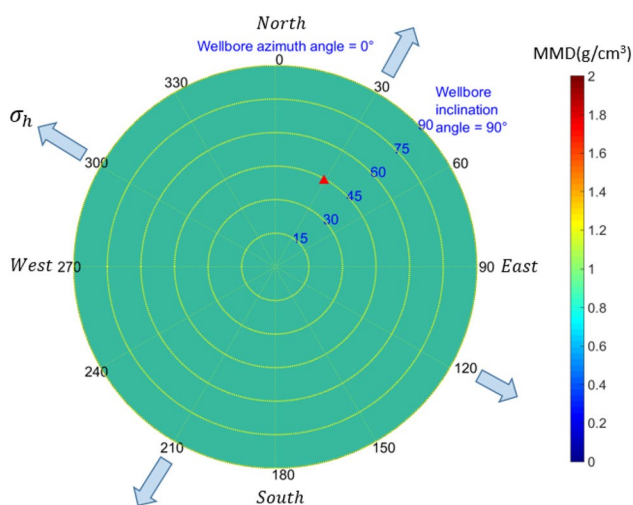


Fig. 7 Hemisphere plot of the minimum mud density (MMD) for all inclined wellbore

tangential stress is between 59 and 120 MPa, whereas for the poroelastodynamics solution, the radial stress is between 18 and 58 MPa and the tangential stress is between 60 and 131 MPa. The significant difference in the stress distribution could indicate the difference in wellbore stability analysis.

4.3 Dynamic Wellbore Stability

The calculation of dynamic wellbore stability is performed according to the flowchart shown in Fig. 4. For wellbore stability analysis, the choice of stress regime, failure criterion, the permeable property of the wellbore, and wellbore depth is significant. Table 3 presents the parameters of in-situ stress regimes. Five stress regimes are considered, including normal fault ($\sigma_v > \sigma_H > \sigma_h$), the transition between normal fault and strike-slip ($\sigma_v = \sigma_H > \sigma_h$), strike-slip ($\sigma_H > \sigma_v > \sigma_h$), the transition between strike-slip and thrust fault ($\sigma_H > \sigma_v = \sigma_h$), and thrust fault ($\sigma_H > \sigma_h > \sigma_v$).

The results of the wellbore stability analysis are presented by the hemisphere plot, as shown in Fig. 7. The direction of maximum horizontal stress is $N30^\circ E$, and the direction of minimum horizontal stress is $N60^\circ W$. The circles with different radii represent different inclination angles, such as 15° , 30° , ..., 90° . For each circle, there are 360° which represent the wellbore azimuth angles. The color bar on the right side shows the different colors that indicate different values of the minimum mud density (MMD) with the unity of g/cm^3 . The color will be distributed on the left figure. Figure 7 shows one simple example, where all the values are set to be $1 \text{ g}/\text{cm}^3$. In this example, the red triangular point means that at a certain depth, for a wellbore with an inclination degree of 45° and an azimuth angle of $N30^\circ E$, the minimum mud density is

$1 \text{ g}/\text{cm}^3$. One point to be noted is that in the hemisphere plot of the minimum mud density (MMD), all the values are the minimum mud density to avoid wellbore collapse (shear failure). As we know, kick is also a serious drilling problem that needs to be avoided; therefore, the wellbore pressure should also be higher than the formation pore pressure. As mentioned by Zoback (2010), if wellbore stability is not a concern in a given area, the minimum mud weight is usually taken to be the pore pressure, so that a well does not flow while drilling. When wellbore stability is a consideration, the lower bound of the mud window is the minimum mud weight required to achieve the desired degree of wellbore stability. In this paper, since the normal pore pressure ($1.01 \text{ g}/\text{cm}^3$) is considered, if the value in the hemisphere plot is less than $1.01 \text{ g}/\text{cm}^3$, the lower bound of the safe mud window should be the pore pressure plus the maximum swab pressure to avoid the kick, rather than the MMD to avoid wellbore collapse. However, in the following analysis, the results are focused on wellbore instability (shear failure) problems.

(1) The influence of failure criteria

Figure 8 is the distribution of minimum mud density (MMD) of different failure criteria for a normal fault. It shows that although different failure criteria could generate different values of MMD, for a certain in-situ stress regime, the distribution of MMD in all these six hemisphere plots are similar, showing that the highest MMD occurs at the maximum horizontal stress direction with the inclination angle of 80° – 90° , whereas the lowest MMD occurs at the minimum horizontal stress direction with the inclination angle about 30° – 45° . Mohr–Coulomb and Hoek–Brown always generate the highest MMD. Many researchers (Zhang 2010; Gholami 2014; Maleki 2014; Ma 2015; Rahimi 2015; Meng 2018, 2019a) have pointed out that these two criteria usually overestimate the rock breakout and provide the highest MMD, because they do not consider the influence of intermediate principal stresses. Instead, Drucker–Prager underestimates the rock breakout and provides the lowest MMD. Leandro Alejandro (2012) conducted thorough research on Drucker–Prager criterion and pointed out that although it is a three-dimensional pressure-dependent model, it consistently overestimates the strength of intact rock, or underestimates the MMD. It is only appropriate for a narrow range of stress in the vicinity of the intermediate and minor principal stress from which the parameters of the criterion are obtained. For the other failure criteria, such as Mogi–Coulomb, Modified Lade, and 3D Hoek–brown, they provide the MMD neither as high as Mohr–Coulomb, nor as low as Drucker–Prager. These three failure criteria seem to be more dependable than Mohr–Coulomb and Hoek–Brown, because they are three-dimensional failure criteria that consider the influence of

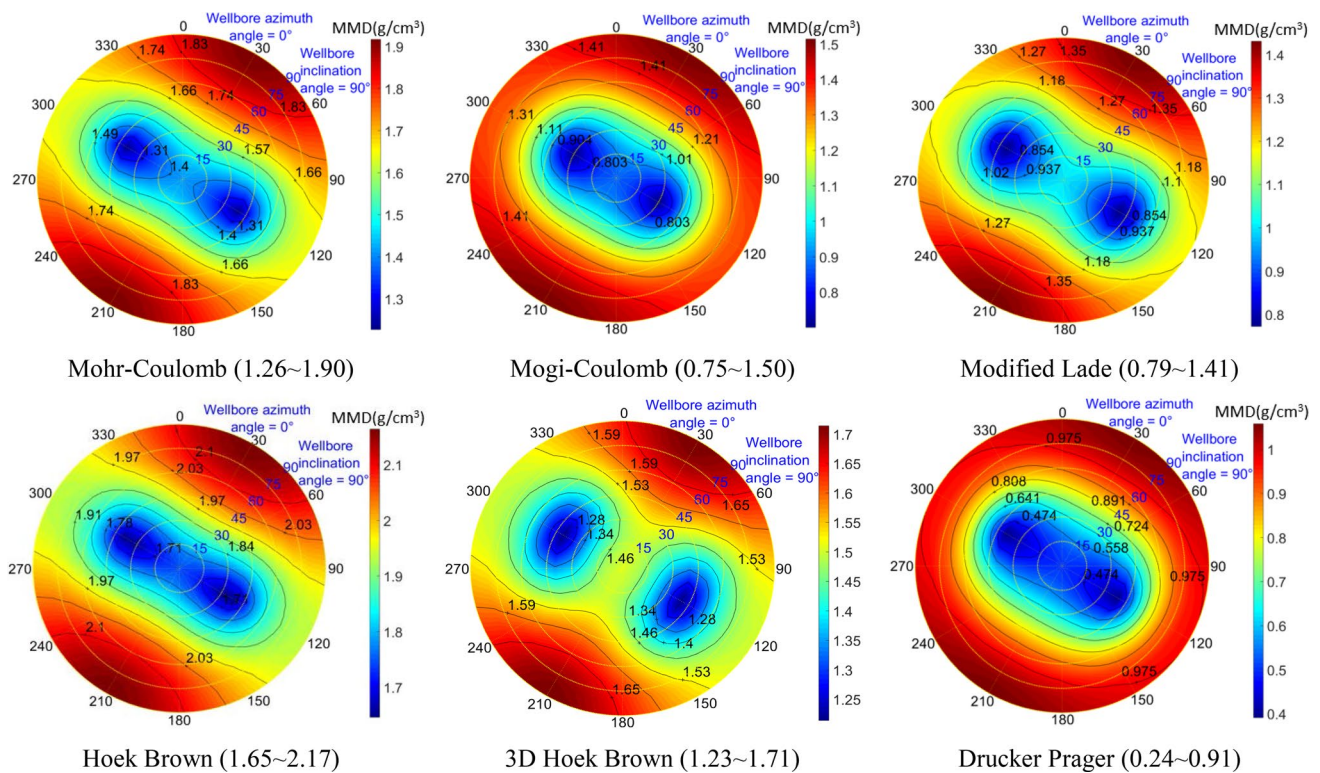


Fig. 8 Distribution of MMD of different failure criteria for normal fault

intermediate principal stresses, which is also proved by Reza Rahimi (2015), Zhang (2010), Bahrami et al. (2017), etc.

However, there are also some minor differences among these three dependable failure criteria. In our analysis, their relationship is $MMD_{3DHoek-Brown} > MMD_{Mogi-Coulomb} > MMD_{Modified\ Lade}$. Researchers do not have uniform opinions for the reliability of these three failure criteria. Since their results are similar, Reza Rahimi (2015) mentioned that they could be used interchangeably. However, other researchers, such as Zhang (2010), mentioned that 3D Hoek-brown and Mogi-Coulomb are better, whereas Modified Lade could generate significant over-prediction. Bahrami (2017) pointed out that the Modified Lade is the best after comparing the failure criteria with polyaxial data. Considering the complexity of the field formation and early researchers' inconsistent conclusions, more cases should be conducted to verify the reliability of these three failure criteria. It is difficult and even impossible to generate the direct relationship between any certain formation and the best choice of failure criteria. To better understand which failure criterion is the best, in Sect. 4.4 of this paper, triaxial compression tests have been performed under dynamic loading conditions to verify the accuracy of different failure criteria. The experimental data could be used to demonstrate whether these failure criteria could be used under dynamic loading conditions and which one is the best.

(2) The influence of in-situ stress regimes

Figure 9 shows the distribution of MMD for different in-situ stress regimes using Modified Lade failure criterion. For different in-situ stress regimes, the distribution of MMD in the hemisphere plot is very different. This demonstrates that the in-situ stress regimes determine the distribution of MMD under various inclination and azimuth angles. The optimal and worst wellbore trajectory under different stress regimes could also be generated.

For the normal fault (NF) stress regime, the worst case, or in other words, the highest required MMD occurs in the maximum horizontal stress direction with a high inclination angle of 75°–90°. They represent horizontal wellbores drilled along the maximum stress direction. If any inclined wellbores are drilled in this stress regime condition, the maximum horizontal stress direction should be avoided. Otherwise, a narrow safe mud window will be encountered, and it increases the difficulty of safe drilling operations. The lowest required MMD occurs in the minimum horizontal stress direction with the inclination angle of about 40°. It is suggested to design the inclined wellbore in the minimum horizontal stress direction from the wellbore stability point of view.

For the transition of the normal fault and strike-slip (NF-SS) stress regime, the worst case also occurs in the maximum horizontal stress direction. The lowest required

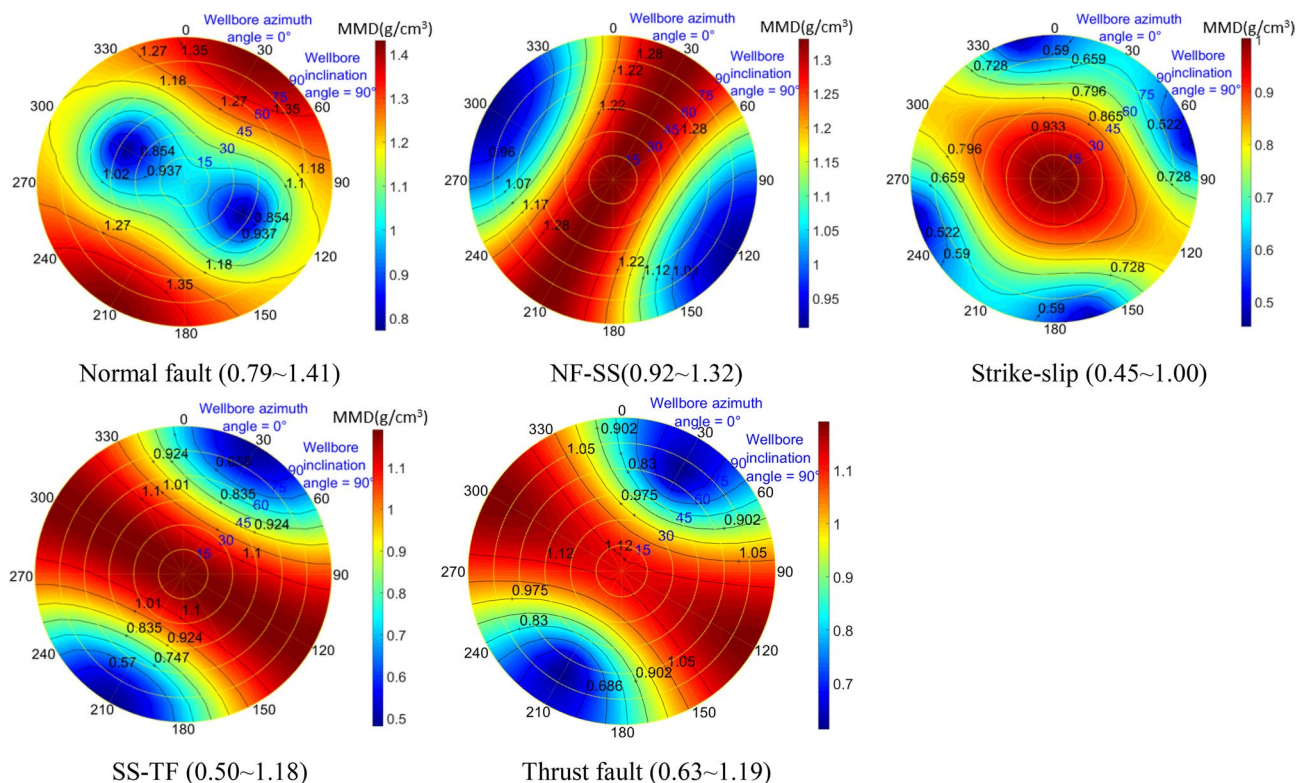


Fig. 9 Distribution of MMD of different in-situ stress regimes using Modified Lade failure criteria

MMD occurs in the minimum horizontal stress direction. However, different from the NF regime, the lowest required MMD occurs in high inclination angles of 90° instead of 40°. Meanwhile, if the maximum horizontal stress direction was designed according to the reservoir simulation, the highest MMD is required for all inclined wellbore, because the inclination angle has little effect on the MMD at this azimuth angle.

For the strike-slip (SS) stress regime, the distribution of MMD is different from all other four stress regimes, because the highest required MMD always occurs in the low inclination angles between 0° and 10°, which indicate the vertical or low inclined wellbores. Within the inclination angle of 15°, the azimuth has little influence

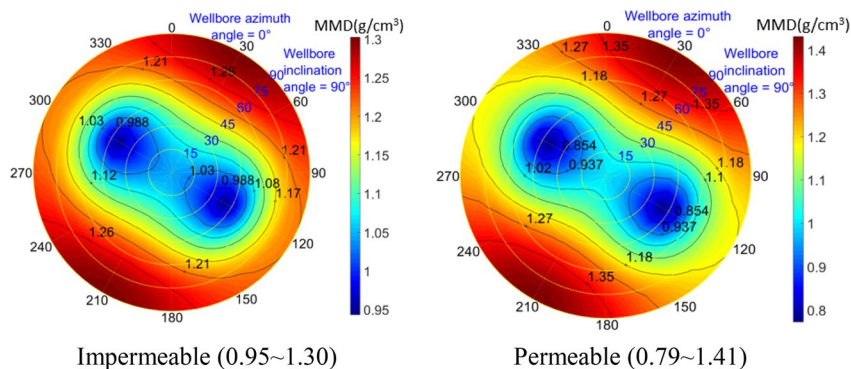
on the distribution of MMD. Different from the NF and NF-SS regimes, the MMD in the maximum horizontal stress direction is smaller than the minimum horizontal stress. The lowest MMD does not occur in the maximum horizontal stress direction. It occurs at four nearly symmetrical azimuth angles of N70°E, S10°E, S70°W, and N10°W with an inclination angle of 90°, which indicate horizontal wellbores.

For the transition of the strike-slip and thrust fault (SS-TF) stress regime, the distribution of the highest and lowest MMD is opposite of the NF-SS regime. The worst case appears in the minimum horizontal stress direction, while the optimal case appears in the maximum horizontal stress direction. It is recommended to design the

Table 4 Optimal and worst wellbore trajectory for different in-situ stress regimes

In-situ stress regimes	The optimal wellbore trajectory			The worst wellbore trajectory		
	$\alpha/(\text{°})$	$\beta/(\text{°})$	Well type	$\alpha/(\text{°})$	$\beta/(\text{°})$	Well type
NF	N45°W–N75°W	30°–45°	Inclined	N20°E–N40°E	80°–90°	Horizontal
NF-SS	N40°W–N80°W	80°–90°	Horizontal	N25°E–N35°E	0°–90°	All type
SS	N70°E, S10°E, S70°W, N10°W	90°	Horizontal	0°–360°	0°–10°	Vertical
SS-TF	N20°E–N40°E	90°	Horizontal	N50°W–N70°W	0°–90°	All type
TF	N20°E–N40°E	60°–75°	Inclined	N50°W–N70°W	75°–90°	Horizontal

Fig. 10 Distribution of MMD of the different permeable property of the wellbore using Modified Lade criteria



inclined wellbore in or close to the maximum horizontal stress direction. Meanwhile, one point to be noted is in the minimum horizontal stress direction, the influence of the inclination angle is trivial; whereas in the maximum horizontal stress direction, the influence of the inclination angle is significant and the MMD decreases as the inclination angle increases.

For the thrust fault (TF) stress regime, as with the SS-TF, the highest MMD occurs in the minimum horizontal stress direction, while the lowest MMD occurs in the maximum horizontal stress direction. In addition, the variance of MMD in the maximum horizontal stress direction is greater than that of the minimum horizontal stress direction. However, unlike the SS-TF, the inclination angle is significant in all azimuth angles for TF. Finally, the summarized optimal and worst drilling direction for these stress regimes are shown in Table 4.

(3) The influence of permeable property of the wellbore

The permeable property of the wellbore could influence the MMD under different inclination and azimuth angles. From Fig. 10, it is found that, compared with the impermeable wellbore, the ranges of the MMD are wider, and the lower bound becomes even lower for the fully permeable

wellbore. In the field, mud cake could buildup on the wellbore surface during drilling because of the residue deposited on the permeable wellbore when the drilling fluid is forced against the wellbore under the wellbore pressure. If the mud cake does not build up or the quality of mud cake is very poor, or the wellbore is during underbalanced drilling, the wellbore could be assumed to be fully permeable. Instead, if the mud cake has built up already and possesses a good sealing effect, the wellbore could be assumed to be impermeable. However, if the mud cake has some permeability and thickness, then its influence on wellbore stability cannot be ignored (Tran 2010; Feng 2018). Fortunately, impermeable and fully permeable wellbores are the two boundaries of the mud cake effect. Before a detailed study of the mud cake effect is provided, it is meaningful to consider these two boundaries at the beginning.

(4) Comparison between the conventional solution and poroelastodynamics solution

The conventional Kirsch solution is widely used to analyze wellbore stability. It is meaningful to compare the wellbore stability analysis based on the newly proposed poroelastodynamics model and the conventional method. Figure 11 demonstrates a comparison between these two

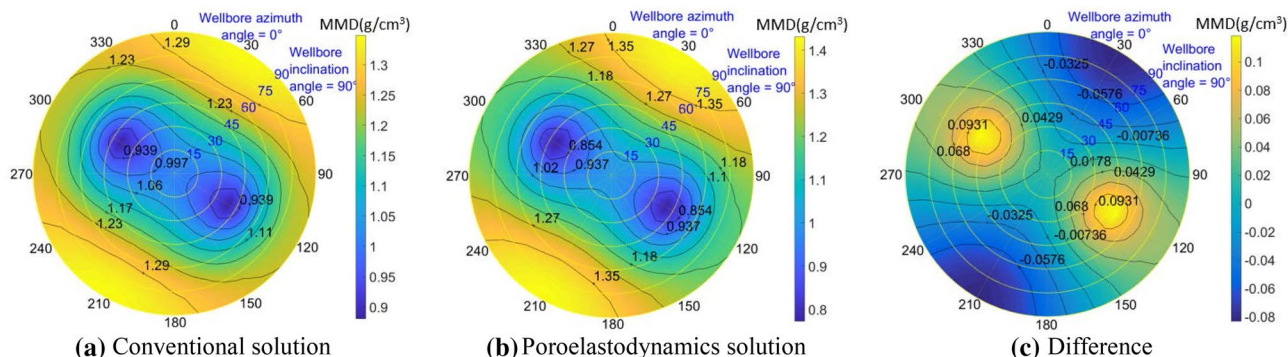


Fig. 11 Comparison between two solutions for Modified Lade under NS stress regime (difference is the conventional solution minus the poroelastodynamics solution)

Table 5 Input parameters for calculation of case II

Parameter	Value	Unit	Parameter	Value	Unit
Wellbore			Formation		
Hole diameter	0.2286	m	Formation pressure	9.81	MPa
Wellbore length	1000	m	Cohesion	8	MPa
Drill pipe length	771.4	m	Internal angle	25	°
Drill pipe OD	0.127	m	Biot coefficient	0.8	–
Drill pipe ID	0.1016	m	Drilling fluid		
Drill collar length	164.592	m	Drilling fluid type	Bingham	
Drill collar OD	0.2032	m	Drilling fluid density	1100	kg/m ³
Drill collar ID	0.127	m	Plastic viscosity	0.045	Pa.s
Surface casing length	542.8	m	Yield value	7.18	Pa
Surface casing OD	0.25654	m			
Surface casing ID	0.23622	m			

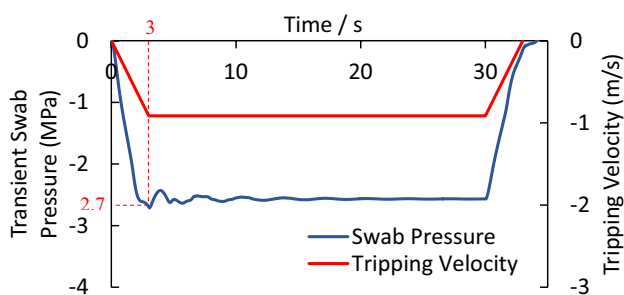


Fig. 12 Tripping velocity, dynamic surge/swab pressure versus time

methods and the Modified Lade failure criteria are applied to both methods. Figure 11a presents the conventional solution, Fig. 11b presents the poroelastodynamics solution, and Fig. 11c presents the difference between these two solutions. Here, the difference is the MMD calculated by the conventional method minus the MMD calculated by the poroelastodynamics model. As shown in this figure, the difference is between -0.08 and 0.11 g/cm³. In the maximum horizontal

stress direction with inclination angles between 30° and 90°, the difference is negative, which indicates that compared with the new poroelastodynamics model, the conventional method underestimates the MMD. In the minimum horizontal stress direction with inclination angles between 15° and 90°, the difference is positive, which indicates that compared with the new poroelastodynamics model, the conventional method overestimates the MMD. Therefore, if the conventional solution was used to analyze wellbore stability under tripping operations, both underestimation and overestimation of MMD will occur. However, one case is not enough to generate conclusions; therefore, another case with a lower depth will be compared.

The second case of a 1000 m depth wellbore is calculated and compared. Table 5 lists the input parameters of the second case. Substituting these parameters into the method presented in Sect. 2.1, the tripping velocity profile and transient swab pressure profile during tripping out could be generated (Fig. 12). The negative value represents that the swab pressure reduces the wellbore pressure. At about 3 s, the absolute transient swab pressure is at a

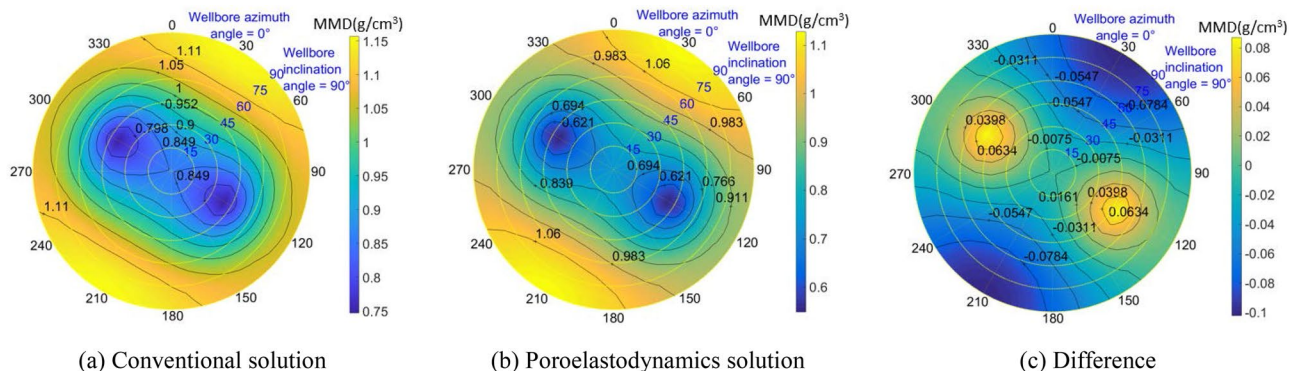


Fig. 13 Comparison between two solutions for Modified Lade under NS stress regime (difference is the conventional solution minus the poroelastodynamics solution)

Table 6 Strength of limestone under different strain rates and confining pressures

Confining pressure/MPa	$1 \times 10^{-6}/s$	$1 \times 10^{-5}/s$	$1 \times 10^{-4}/s$
0	29.2	34.9	41.8
6.9	53.2	55.6	57.9
13.8	62.7	67.4	73.3
20.7	79.2	85.2	84.6

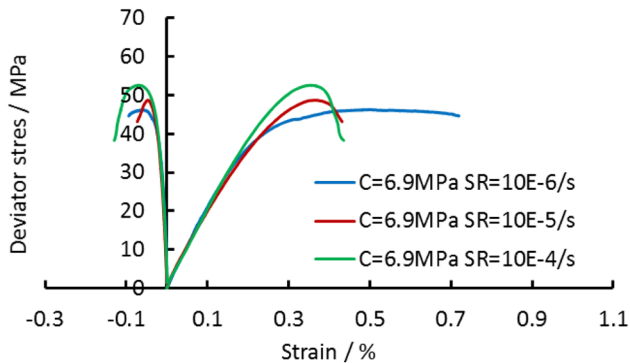


Fig. 14 Stress–strain curves under 6.9 MPa confining pressure and different strain rates

maximum of 2.7 MPa. The wellbore stress will be calculated at this moment.

Figure 13 shows the comparison between the conventional solution and the poroelastodynamics solution for case II. Such as in case I, compared with the new poroelastodynamics model, the conventional method could both overestimate and underestimate the MMD. The difference is between -0.1 and 0.08 g/cm^3 . The overestimation occurs in the minimum horizontal stress direction with the inclination angle of 15° and 90° , whereas the underestimation occurs in the maximum horizontal stress direction with the inclination angle of 30° – 90° .

Through these two cases, it is found that the MMD predicted by the poroelastodynamics model can be significantly different from the conventional solution. The difference can be higher than 0.1 g/cm^3 . Compared with the poroelastodynamics solution, the conventional solution could both overestimate and underestimate the MMD. In this paper, the poroelastodynamics model is strictly derived from the basic poroelastic equations. It can not only simulate the coupling effect between deformation and fluid seepage, but also consider the inertia effect under dynamic loading conditions. The conventional solution based on the Kirsch solution provided by Chen (2008), also used by Ma (2015) and many other researchers is a simplified calculation considering the fluid seepage effect. Therefore, it is reasonable to assume that the solution of the poroelastodynamics model is more

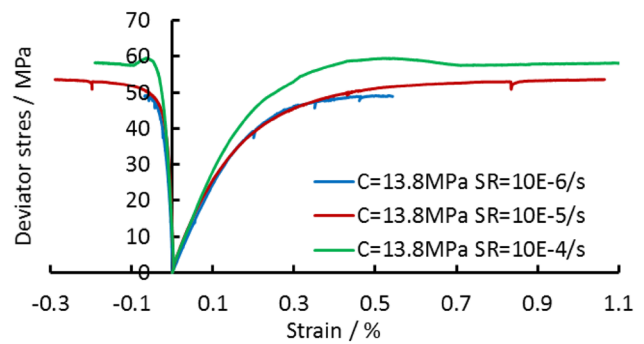


Fig. 15 Stress–strain curves under 13.8 MPa confining pressure and different strain rates

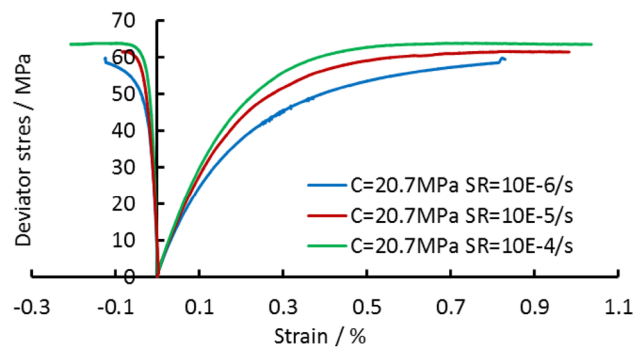


Fig. 16 Stress–strain curves under 20.7 MPa confining pressure and different strain rates

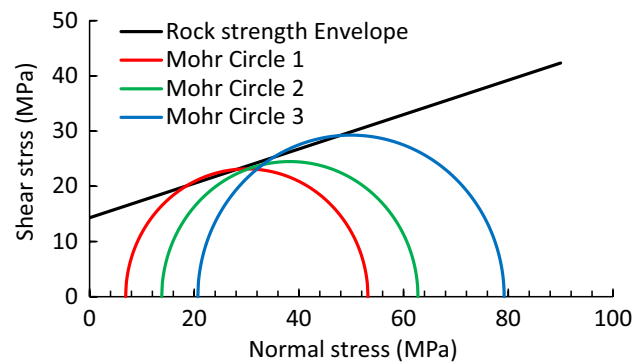


Fig. 17 Generation of rock cohesion and internal angle

accurate than the conventional solution provided by Chen (2008). In both cases, overestimation occurs in the minimum horizontal stress direction with the inclination angle between 15° and 90° , whereas underestimation occurs in the maximum horizontal stress direction with the inclination angle between 30° and 90° . Therefore, to get a more accurate MMD during tripping operations, the poroelastodynamics model should be used.

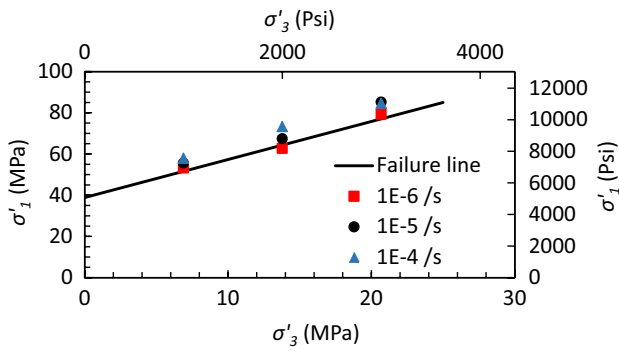


Fig. 18 Mohr–Coulomb failure criterion (solid line), fitted to triaxial test data

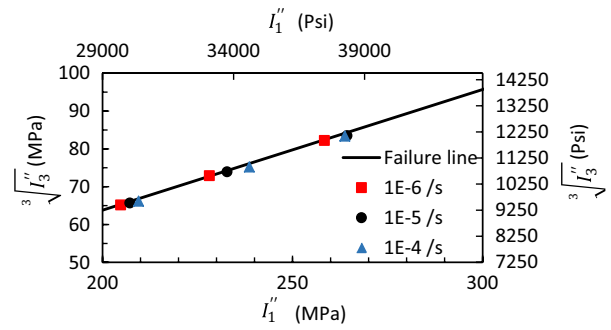


Fig. 21 Modified Lade failure criterion (solid line), fitted to triaxial test data

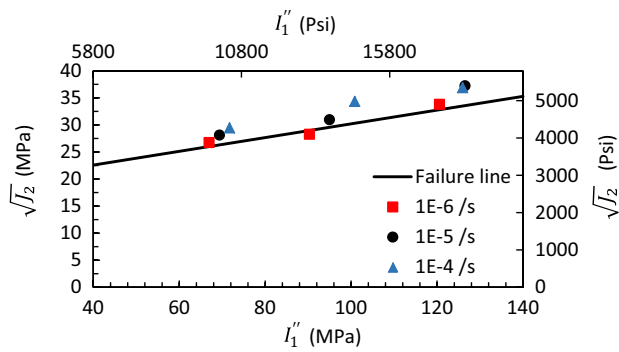


Fig. 19 Circumscribed Drucker–Prager failure criterion (solid line), fitted to triaxial test data

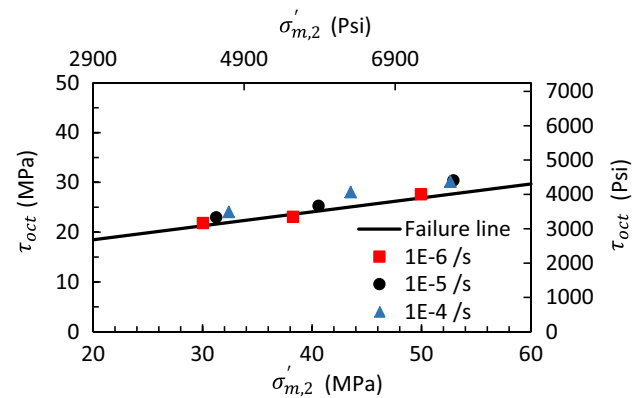


Fig. 22 Mogi–Coulomb failure criterion (solid line), fitted to triaxial test data

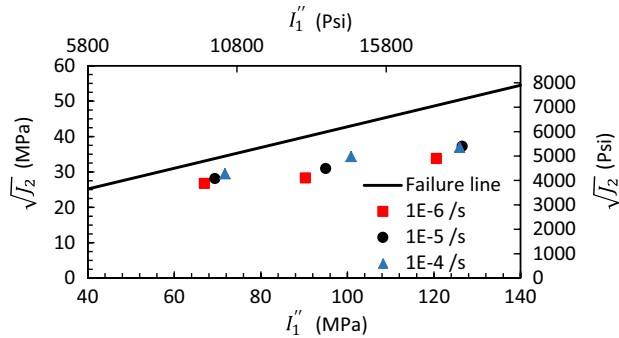


Fig. 20 Inscribed Drucker–Prager failure criterion (solid line), fitted to triaxial test data

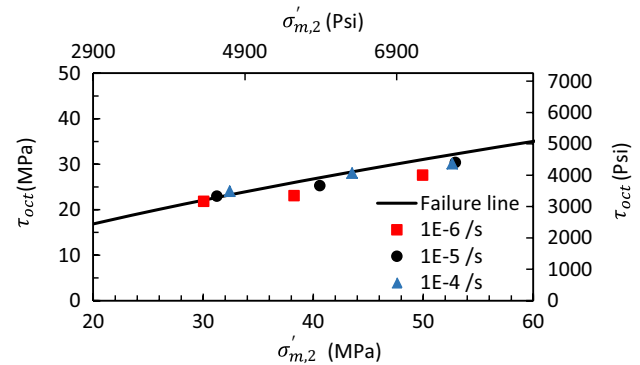


Fig. 23 3D Hoek–Brown failure criterion (solid line), fitted to triaxial test data

4.4 Experimental Validation

Table 6 shows the triaxial compression strength of Bedford limestone under different strain rates and confining pressure. The stress–strain curves are presented from Figs. 14, 15 and 16. It shows that the rock strength increases

with confining pressure at the same strain rate. Meanwhile, at the same confining pressure, the rock strength increases with the strain rate. This is consistent with the

experimental results provided by many other researchers (Lajtai et al. 1991; Li et al. 1999; Mahmutoglu 2006; Liang et al. 2015). However, none of these researchers provided enough experimental data or used the data to check the accuracy of different static failure criteria under dynamic loading conditions.

The experimental data with different confining pressures under the strain rate of $10^{-6}/s$ were chosen to generate rock cohesion and internal angle, which are presented in Fig. 17. The rock cohesion is optimized to be 14.3 MPa and the internal angle is 17.3° . The reason that the data under the strain rate of $10^{-6}/s$ were used is that they are regarded as the static rock properties. After the rock cohesion and internal angle are calculated, the constitutive relationship of different failure criteria and experimental data could be plotted together, as shown in Figs. 18, 19, 20, 21, 22 and 23. The constitutive relationship of each failure criteria is different, therefore, the x -axis and y -axis are varied for different plots (Ulusay 2014). It is not quite reliable to compare the accuracy of different failure criteria by only looking at these graphs. The reasonable method should be proposed to evaluate the accuracy of prediction.

Zhang (2010) has introduced prediction errors to check the accuracy of different failure criteria with polyaxial compression data under static loading conditions. Based on Zhang’s work, two modified non-dimensional numbers are introduced to calculate the prediction errors:

$$\text{Diff}_{\text{ave}} = 100 \frac{\sum_{i=1}^n \left\{ \left[(\sigma'_1)_{\text{pre}} \right]_i - \left[(\sigma'_1)_{\text{exp}} \right]_i \right\}}{n \cdot \text{UCS}}, \tag{15}$$

$$\text{Diff}_{\text{abs}} = 100 \frac{\sum_{i=1}^n \left\{ \left| \left[(\sigma'_1)_{\text{pre}} \right]_i - \left[(\sigma'_1)_{\text{exp}} \right]_i \right\}}{n \cdot \text{UCS}}, \tag{16}$$

where $\left[(\sigma'_1)_{\text{pre}} \right]_i$ and $\left[(\sigma'_1)_{\text{exp}} \right]_i$ are, respectively, the predicted and experimental major principal stresses at failure for all data points; n represents the total number of data points; UCS is the uni-axial rock strength, and it is used to make the prediction difference to be a non-dimensional number; Diff_{ave} is a non-dimensional number that represents the average prediction difference which can be used to indicate whether these failure criteria overestimate or underestimate the rock strength, the positive number of Diff_{ave} represents overestimation; Diff_{abs} is a non-dimensional number that represents the average absolute difference which can be used to indicate how close the predicted and experimental strength values are with each other. The smaller number of Diff_{abs} and Diff_{ave} , the more accurate of the prediction.

According to average prediction errors in Table 7, Mohr–Coulomb significantly underestimates the rock strength, because Diff_{ave} is a relatively small negative

number. Inscribed Drucker–Prager significantly overestimates the rock strength, since Diff_{ave} is a relatively large positive number. The circumscribed Drucker–Prager underestimates the rock strength, but it is not so significant as Mohr–Coulomb. The Mogi–Coulomb only slightly underestimates the rock strength, whereas the Modified Lade and the 3D Hoek–Brown slightly overestimates the rock strength. For the absolute errors in Table 7, Modified Lade has the highest accuracy, whereas the inscribed Drucker–Prager has the lowest accuracy. The accuracy sequence is Modified Lade > 3D Hoek–Brown > Mogi–Coulomb > Circumscribed Drucker–Prager > Mohr–Coulomb > Inscribed Drucker–Prager. If we look back to Figs. 18, 19, 20, 21, 22 and 23, the experimental points lie very close to the constitutive failure line for Modified Lade. Therefore, it shows that when the strain rate is less than $10^{-4}/s$, which is the range of strain rate caused by tripping operations, the static failure criteria, especially the modified Lade, could be used to describe rock failure. It verifies that our theoretical calculation of using Modified Lade failure criteria to predict wellbore stability under tripping operations is valid. Due to the time and materials’ limit, only Bedford limestone was used in our test. The same tests are needed to be repeated on many different types of rocks to prove the accuracy of the Modified Lade failure criteria in the future.

5 Concluding Remarks

Based on the above analysis, several interesting conclusions can be made. A new poroelastodynamics model has been established to analyze wellbore stability under dynamic loading conditions. Compared with the conventional Kirsch solution, this model can simulate the coupled effect of deformation–diffusion in the porous medium under dynamic loading conditions. The model is solved by the finite-difference method with the specific swab pressure caused by tripping operations as the dynamic loading source. The hemisphere plots of the distribution of MMD are provided to present the wellbore stability results.

The results of wellbore stability analysis show that failure criterion, in-situ stress regime, and the permeable property of the wellbore could influence the distribution of MMD. The in-situ stress regime could determine the distribution of MMD under various inclination and azimuth angles. The optimal and worst wellbore trajectory for different in-situ stress regimes is also generated. The three-stress dependent failure criteria, Modified Lade, Mogi–Coulomb, and 3D Hoek–Brown are better than the two-stress dependent failure criteria, Mohr–Coulomb, and Hoek–Brown, to get reasonable MMD. For the fully permeable wellbore, the range of MMD in the hemisphere plot is broader than that of the impermeable wellbore.

For the experimental part, the triaxial compression tests under different strain rate and confining pressure have been performed on Bedford limestone. The results have been used to check the applicability and accuracy of different conventional failure criteria under dynamic loading conditions. This analysis proves that when the strain rate is less than $10^{-4}/s$, which is the range of strain rate caused by tripping operations, the static failure criteria (especially the modified Lade) could be used to describe rock failure.

Two specific cases are used to compare the results of the conventional method and the poroelastodynamics model. Using Modified Lade failure criteria, it shows that compared with the newly developed poroelastodynamics model, the conventional method could either overestimate or underestimate the MMD and the difference can be as significant as 0.11 g/cm^3 . In both cases, overestimation occurs in the minimum horizontal stress direction with the inclination angle of $15^\circ\text{--}90^\circ$, whereas underestimation occurs in the maximum horizontal stress direction with the inclination angle of $30^\circ\text{--}90^\circ$.

In future studies, there are several aspects to be improved. First, experimental data of the other kinds of rocks should be provided to check the accuracy and applicability of different failure criteria under different strain rates. Second, apart from the surge/swab pressure caused by tripping operations, there are many sources of dynamic loading within the wellbore, such as the pressure fluctuations caused by hydraulic fracturing, seismic waves caused by earthquakes, etc. The behavior of wellbores under these dynamic loading conditions is also highly interested. Third, the poroelastodynamics model should be modified to consider fluid inertia. Under high-frequency dynamic loading conditions, both solid inertia and fluid inertia could influence the mechanical behavior of a porous medium. Finally, a more advanced and accurate surge/swab pressure prediction model is expected to be applied in the dynamic wellbore stability analysis under tripping operations.

Appendix

A1 Numerical Solution Strategy of the Poroelastodynamics Model

For the governing equations of the poroelastodynamics model, the numerical solving method is preferred to be used. The reason is, on one hand, the pore pressure term in the displacement equation makes it difficult to find the analytical solution. On the other hand, the analytical solution is not suitable, since the dynamic surge/swab pressure changes arbitrarily which cannot be simulated simply by any specific function. To avoid the redundant unit conversion, non-dimensional quantities should be introduced to modify Eq. (12).

$$\begin{aligned} \text{Non-dimensional distance: } \xi &= \frac{r}{r_w} \\ \text{Non-dimensional displacement: } \phi &= \frac{2G}{\rho_0} \cdot \frac{u_r}{r_w} \\ \text{Non-dimensional pore pressure: } \chi &= \frac{p}{\rho_0} \\ \text{Non-dimensional time: } \tau &= \frac{ct}{r_w} \\ \text{Non-dimensional radial stress: } S_r &= \frac{\sigma_r}{\rho_0} \end{aligned}$$

Introducing these non-dimensional quantities into Eq. (12):

$$\begin{cases} \frac{\partial^2 \phi}{\partial \xi^2} + \frac{1}{\xi} \frac{\partial \phi}{\partial \xi} - \frac{\phi}{\xi^2} - \alpha \frac{1-2\nu}{1-\nu} \frac{\partial \chi}{\partial \xi} = \frac{\partial^2 \phi}{\partial \tau^2} \\ \frac{\partial^2 \chi}{\partial \xi^2} + \frac{1}{\xi} \frac{\partial \chi}{\partial \xi} = \frac{c \dot{r}_w}{c_v} \frac{\chi}{\partial \tau} \end{cases} \quad (17)$$

The implicit difference method is used to differentiate the diffusion equation:

$$\begin{cases} \frac{\partial^2 \chi}{\partial \xi^2} + \frac{1}{\xi} \frac{\partial \chi}{\partial \xi} = \frac{c \cdot r_w}{c_v} \frac{\partial \chi}{\partial \tau} \\ \chi(1, \tau) = f\left(g \frac{r_w}{c} \tau\right) \\ \chi(\infty, \tau) = 0 \\ \chi(\xi, 0) = 0 \end{cases} \quad (18)$$

Since the governing equation is in cylindrical coordinates, it is better to transform the radial direction into Cartesian coordinates. The way is as follows:

$$\xi = \xi_w e^x \quad (19)$$

Then, the diffusion equation in Eq. (18) becomes

$$\frac{\partial^2 \chi}{\partial x^2} = \xi^2 \frac{c \cdot r_w}{c_v} \frac{\partial \chi}{\partial \tau} = \xi_w e^{2x} \frac{c \cdot r_w}{c_v} \frac{\partial \chi}{\partial \tau} \quad (20)$$

Therefore, the implicit finite differential formula of Eq. (20) is

$$\frac{\chi_{i-1}^{n+1} - 2\chi_i^{n+1} + \chi_{i+1}^{n+1}}{(\Delta x)^2} = \left(\xi_w e^{2ix} \frac{c \cdot r_w}{c_v} \right) \frac{\chi_i^{n+1} - \chi_i^n}{\Delta t} \quad (21)$$

Through some derivations, we have

$$\begin{bmatrix} -l_1 & 1 & & & & & \\ 1 & -l_2 & 1 & & & & \\ & \vdots & \ddots & & & & \\ & & & \ddots & & & \\ & & & & 1 & -l_{m-2} & 1 \\ & & & & & 1 & -l_{m-1} \end{bmatrix} \begin{bmatrix} \chi_1^{n+1} \\ \chi_2^{n+1} \\ \vdots \\ \chi_{m-2}^{n+1} \\ \chi_{m-1}^{n+1} \end{bmatrix} = \begin{bmatrix} d_1 - f[\omega(n+1)] \\ d_2 \\ \vdots \\ d_{m-2} \\ d_{m-1} \end{bmatrix} \quad (22)$$

Implicit finite-difference method is also used to differentiate the displacement equation:

$$\begin{cases} \frac{\partial^2 \phi}{\partial \xi^2} + \frac{1}{\xi} \frac{\partial \phi}{\partial \xi} - \frac{\phi}{\xi^2} - \alpha \frac{1-2\nu}{1-\nu} \frac{\partial \chi}{\partial \xi} = \frac{\partial^2 \phi}{\partial \tau^2} \\ f[\omega(n+1)\Delta\tau] = \frac{1-\nu}{1-2\nu} \frac{\partial \phi}{e^x \partial x} \Big|_{(x=0)} + \frac{\nu}{1-2\nu} \frac{\phi}{e^x} \Big|_{(x=0)} - \alpha \chi \\ 0 = \frac{1}{e^x} \Big|_{(x=0)} \left(\frac{1-\nu}{1-2\nu} \frac{\partial \phi}{\partial x} + \frac{\nu}{1-2\nu} \phi \right) - \alpha \chi \\ \phi(x, 0) = 0 \end{cases} \tag{23}$$

Using Eq. (19), the displacement equation in Eq. (23) could be converted into

$$\frac{1}{e^2} \frac{\partial^2 \phi}{\partial x^2} - \frac{\phi}{e^{2x}} - \alpha \frac{1-2\nu}{1-\nu} \frac{\partial \chi}{e^x \partial x} = \frac{\partial^2 \phi}{\partial \tau^2} \tag{24}$$

Therefore, the implicit finite differential formula of Eq. (24) is

$$\begin{aligned} \frac{1}{e^{2i\Delta x}} \frac{\phi_i^{n+1} - 2\phi_i^n + \phi_i^{n-1}}{(\Delta x)^2} - \frac{\phi_i^{n+1}}{e^{2i\Delta x}} - \alpha \frac{1-2\nu}{1-\nu} \frac{\chi_{i+1}^{n+1} - \chi_{i+1}^n}{e^{i\Delta x} \cdot \Delta x} \\ = \frac{\phi_i^{n+1} - 2\phi_i^n + \phi_i^{n-1}}{(\Delta \tau)^2} \end{aligned} \tag{25}$$

$$\begin{bmatrix} B-L_1 & 1 & & & & \\ 1 & -L_2 & 1 & & & \\ & \vdots & & \ddots & & \\ & & & & 1-L_{m-2} & 1 \\ & & & & 1 & C_n-L_{m-1} \end{bmatrix} \begin{bmatrix} \phi_1^{n+1} \\ \phi_2^{n+1} \\ \vdots \\ \phi_{m-2}^{n+1} \\ \phi_{m-1}^{n+1} \end{bmatrix} = \begin{bmatrix} E_1 - A_n \\ E_1 \\ \vdots \\ E_{m-2} \\ E_{m-1} - D_n \end{bmatrix} \tag{26}$$

$$L_i = \frac{1 + \frac{2(\Delta\tau)^2}{e^{2i\Delta x}(\Delta x)^2} - \frac{(\Delta\tau)^2}{e^{2i\Delta x}}}{\frac{(\Delta\tau)^2}{e^{2i\Delta x}(\Delta x)^2}}$$

Table 7 Strength parameters and prediction errors for limestone

Failure criteria	Diff _{ave}	Diff _{abs}
Mohr Coulomb	-11.51	12.40
Circumscribed Drucker-Prager	-5.17	5.58
Inscribed Drucker-Prager	25.51	25.51
Modified Lade	1.16	1.16
Mogi-Coulomb	-3.80	4.11
3D Hoek-Brown	3.29	3.87

$$E_i = \frac{1}{\frac{(\Delta\tau)^2}{e^{2i\Delta x}(\Delta x)^2}} \left[\phi_i^{n-1} - 2\phi_i^n + \alpha \frac{1-2\nu}{1-\nu} \frac{(\Delta\tau)^2}{e^{2i\Delta x} \Delta x} (\chi_{i+1}^{n+1} - \chi_i^{n+1}) \right]$$

$$A_n = \frac{(1+\alpha)\sin[\omega(n+1)\tau]}{\frac{\nu}{1-2\nu} - \frac{1-\nu}{1-2\nu} \frac{1}{\Delta x}}, B = \frac{-\frac{1-\nu}{1-2\nu} \frac{1}{\Delta x}}{\frac{\nu}{1-2\nu} - \frac{1-\nu}{1-2\nu} \frac{1}{\Delta x}},$$

$$C_n = \frac{\frac{1-\nu}{1-2\nu} \frac{1}{\Delta x}}{\frac{\nu}{1-2\nu} + \frac{1-\nu}{1-2\nu} \frac{1}{\Delta x}}, D_n = \frac{\alpha \chi_m^{n+1}}{\frac{\nu}{1-2\nu} + \frac{1-\nu}{1-2\nu} \frac{1}{\Delta x}}$$

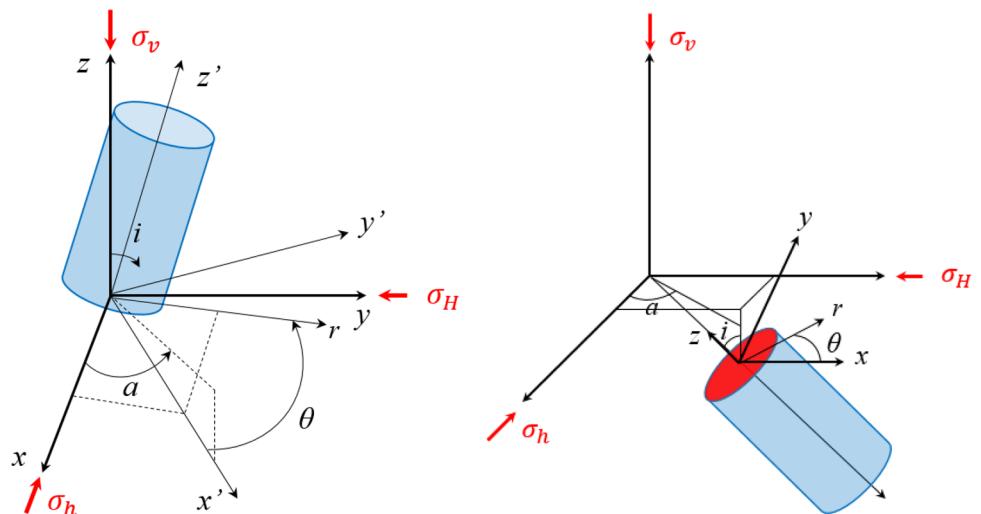
The tridiagonal matrix algorithm (TDMA), also known as the Thomas algorithm, is a simplified form of Gaussian elimination that can be used to solve Eqs. (22) and (26)

After rearrangement, we have

A2 Conventional Method of Calculating Wellbore Stress

The in-situ stress of the virgin formation for a deviated well is as follows (Fig. 24):

Fig. 24 Diagram of directional well



$$\begin{bmatrix} \sigma_x^0 \\ \sigma_y^0 \\ \sigma_z^0 \end{bmatrix} = \begin{bmatrix} \cos^2 a \cdot \cos^2 i & \sin^2 a \cdot \cos^2 i & \sin^2 i \\ \sin^2 a & \cos^2 a & 0 \\ \cos^2 a \cdot \sin^2 i & \sin^2 a \cdot \sin^2 i & \cos^2 i \end{bmatrix} \begin{bmatrix} \sigma_H \\ \sigma_h \\ \sigma_v \end{bmatrix}$$

$$\begin{bmatrix} \sigma_{xy} \\ \sigma_{xz} \\ \sigma_{yz} \end{bmatrix} = \frac{1}{2} \begin{bmatrix} -\sin 2a \cdot \cos i & \sin 2a \cdot \cos i & 0 \\ \cos^2 a \cdot \sin 2i & \sin^2 a \cdot \sin 2i & -\sin 2i \\ -\sin 2a \cdot \sin i & \sin 2a \cdot \sin i & 0 \end{bmatrix} \begin{bmatrix} \sigma_H \\ \sigma_h \\ \sigma_v \end{bmatrix} \quad (27)$$

Under static loading conditions, the conventional solution for impermeable wellbore is provided by Fjar et al. (2008). It is very well-known and not include here. The conventional solution for permeable wellbore is (Chen 2008; Ma 2015)

$$\begin{aligned} \sigma_r &= \left(\frac{\sigma_x^0 + \sigma_y^0}{2} \right) \left(1 - \frac{r_w^2}{r^2} \right) \\ &+ \left(\frac{\sigma_x^0 - \sigma_y^0}{2} \right) \left(1 + \frac{3r_w^4}{r^4} - \frac{4r_w^2}{r^2} \right) \cos 2\theta \\ &+ \sigma_{xy} \left(1 + \frac{3r_w^4}{r^4} - \frac{4r_w^2}{r^2} \right) \sin 2\theta + P_w \frac{r_w^2}{r^2} \\ &+ \left[\frac{\alpha(1-2\nu)}{2(1-\nu)} \left(1 - \frac{r_w^2}{r^2} \right) - \emptyset \right] (p_i - p_p) - \alpha p_p \\ \sigma_\theta &= \left(\frac{\sigma_x^0 + \sigma_y^0}{2} \right) \left(1 + \frac{r_w^2}{r^2} \right) - \left(\frac{\sigma_x^0 - \sigma_y^0}{2} \right) \left(1 + \frac{3r_w^4}{r^4} \right) \cos 2\theta \\ &- \sigma_{xy} \left(1 + \frac{3r_w^4}{r^4} \right) \sin 2\theta - P_w \frac{r_w^2}{r^2} \\ &+ \left[\frac{\alpha(1-2\nu)}{2(1-\nu)} \left(1 - \frac{r_w^2}{r^2} \right) - \emptyset \right] (p_i - p_p) - \alpha p_p \quad (28) \\ \sigma_z &= \sigma_z^0 - \nu \left[\frac{2r_w^2}{r^2} (\sigma_H - \sigma_h) \cos 2\theta + 4\sigma_{xy} \frac{r_w^2}{r^2} \sin 2\theta \right] \\ &+ \left[\frac{\alpha(1-2\nu)}{2(1-\nu)} \left(1 - \frac{r_w^2}{r^2} \right) - \emptyset \right] (p_i - p_p) - \alpha p_p \\ \sigma_{r\theta} &= \left(\frac{\sigma_x^0 - \sigma_y^0}{2} \right) \left(1 - \frac{3r_w^4}{r^4} + \frac{2r_w^2}{r^2} \right) \sin 2\theta \\ &+ \sigma_{xy} \left(1 - \frac{3r_w^4}{r^4} + \frac{2r_w^2}{r^2} \right) \cos 2\theta \\ \sigma_{\theta z} &= (-\sigma_{xz} \sin \theta + \sigma_{yz} \cos \theta) \left(1 + \frac{r_w^2}{r^2} \right) \end{aligned}$$

$$\sigma_{rz} = (\sigma_{xz} \cos \theta + \sigma_{yz} \sin \theta) \left(1 - \frac{r_w^2}{r^2} \right),$$

where p_0 is the static wellbore pressure, and \emptyset is the porosity.

References

- Aadnoy BS, Chenevert ME (1987) Stability of highly inclined boreholes (includes associated papers 18596 and 18736). *SPE Drill Eng* 2:364–374. <https://doi.org/10.2118/16052-PA>
- Al-Ajmi A (2006) Wellbore stability analysis based on a new true-triaxial failure criterion. Dissertation, KTH Royal Institute of Technology
- Al-Ajmi AM, Zimmerman RW (2005) Relation between the Mogi and the Coulomb failure criteria. *Int J Rock Mech Min Sci* 42:431–439. <https://doi.org/10.1016/j.ijrmms.2004.11.004>
- Alejano LR, Bobet A (2012) Drucker–Prager criterion. *Rock Mech Rock Eng* 45:995–999. <https://doi.org/10.1007/s00603-012-0278-2>
- Bahrami B, Mohsenpour S, Miri MA, Mirhaseli R (2017) Quantitative comparison of fifteen rock failure criteria constrained by polyaxial test data. *J Petrol Sci Eng* 159:564–580. <https://doi.org/10.1016/j.petrol.2017.09.065>
- Bradley WB (1979) Failure of inclined boreholes. *J Energy Resour Technol* 101:232–239. <https://doi.org/10.1115/1.3446925>
- Burkhardt JA (1961) Wellbore pressure surges produced by pipe movement. *J Petrol Technol* 13:595–605. <https://doi.org/10.2118/1546-G-PA>
- Cai M, Kaiser PK, Suorineni F, Su K (2007) A study on the dynamic behavior of the Meuse/Haute-Marne argillite. *Phys Chem Earth* 32:907–916. <https://doi.org/10.1016/j.pce.2006.03.007>
- Cannon GE (1934) Changes in hydrostatic pressure due to withdrawing drill pipe from the hole. In: *Drill and production practice*. American Petroleum Institute
- Chen M, Jin Y (2008) *Rock mechanics in petroleum engineering*. Science Press, China (Chinese edition)
- Crespo FE, Ramadan MA, Arild S, Majed E, Mahmood A (2012) Surge-and-swab pressure predictions for yield-power-law drilling fluids. *SPE Drill Complet* 27:574–585
- Detournay E, Cheng AD (1988) Poroelastic response of a borehole in a non-hydrostatic stress field. *Int J Rock Mech Min Sci Geomech Abstr* 25:171–182. [https://doi.org/10.1016/0148-9062\(88\)92299-1](https://doi.org/10.1016/0148-9062(88)92299-1)
- Ewy RT (1999) Wellbore-stability predictions by use of a modified Lade criterion. *SPE Drill Complet* 14:85–91. <https://doi.org/10.2118/56862-PA>
- Fairhurst C (1967) Methods of determining in-situ rock stresses at great depths. Missouri River Division, US Army, Jefferson City
- Feng Y, Li X, Gray KE (2018) An easy-to-implement numerical method for quantifying time-dependent mudcake effects on near-wellbore stresses. *J Pet Sci Eng* 164:501–514
- Fjar E, Ruistuen H (2002) Impact of the intermediate principal stress on the strength of heterogeneous rock. *J Geophys Res Solid Earth* 107:ECV–E3. <https://doi.org/10.1029/2001JB000277>
- Fjar E, Holt RM, Raaen AM, Risnes R, Horsrud P (2008) *Petroleum related rock mechanics*. Elsevier, Amsterdam
- Fontenot JE, Clark RK (1974) An improved method for calculating swab and surge pressures and circulating pressures in a drilling well. *Soc Pet Eng J* 14:451–462. <https://doi.org/10.2118/4521-PA>
- Gholami R, Moradzadeh A, Rasouli V, Hanachi J (2014) Practical application of failure criteria in determining safe mud weight

- windows in drilling operations. *J Rock Mech Geotech Eng* 6:13–25. <https://doi.org/10.1016/j.jrmge.2013.11.002>
- Handin J, Heard HA, Magouirk JN (1967) Effects of the intermediate principal stress on the failure of limestone, dolomite, and glass at different temperatures and strain rates. *J Geophys Res* 72(2):611–640. <https://doi.org/10.1029/JZ072i002p00611>
- Islam MA, Skalle P, Al-Ajmi AM, Soreide OK (2010) Stability analysis in shale through deviated boreholes using the Mohr and Mogi-Coulomb failure criteria. In: 44th US rock mechanics symposium and 5th US–Canada rock mechanics symposium. American Rock Mechanics Association
- Jaeger JC, Cook NG, Zimmerman R (2009) *Fundamentals of Rock Mechanics*. Wiley, Oxford
- Karlsen AG (2014) Surge and swab pressure calculation: calculation of surge and swab pressure changes in laminar and turbulent flow while circulating mud and pumping. Master thesis, Institutt for petroleumsteknologi og anvendt geofysikk
- Lajtai EZ, Duncan ES, Carter BJ (1991) The effect of strain rate on rock strength. *Rock Mech Rock Eng* 24:99–109. <https://doi.org/10.1007/BF01032501>
- Li HB, Zhao J, Li TJ (1999) Triaxial compression tests on a granite at different strain rates and confining pressures. *Int J Rock Mech Min Sci* 36:1057–1063. [https://doi.org/10.1016/S1365-1609\(99\)00120-3](https://doi.org/10.1016/S1365-1609(99)00120-3)
- Liang C, Wu S, Li X, Xin P (2015) Effects of strain rate on fracture characteristics and mesoscopic failure mechanisms of granite. *Int J Rock Mech Min Sci* 76: 146–154. <https://doi.org/10.1016/j.ijrmmms.2015.03.010>
- Lubinski A (1988) *Developments in petroleum engineering*. Gulf Publishing Company, Houston
- Lubinski A, Hsu FH, Nolte KG (1977) Transient pressure surges due to pipe movement in an oil well. *Oil Gas Sci Technol* 32:307–348. <https://doi.org/10.2516/ogst:1977019>
- Ma T, Chen P, Yang C, Zhao J (2015) Wellbore stability analysis and well path optimization based on the breakout width model and Mogi–Coulomb criterion. *J Pet Sci Eng* 135:678–701. <https://doi.org/10.1016/j.petrol.2015.10.029>
- Mahmutoğlu Y (2006) The effects of strain rate and saturation on a macro-cracked marble. *Eng Geol* 82:137–144. <https://doi.org/10.1016/j.enggeo.2005.09.001>
- Maleki S, Gholami R, Rasouli V, Moradzadeh A, Riabi RG, Sadaghzadeh F (2014) Comparison of different failure criteria in prediction of safe mud weigh window in drilling practice. *Earth Sci Rev* 136:36–58. <https://doi.org/10.1016/j.earscirev.2014.05.010>
- Meng M, Qiu ZS (2018) Experiment study of mechanical properties and microstructures of bituminous coals influenced by supercritical carbon dioxide. *Fuel* 219:223–238
- Meng M, Baldino S, Miska SZ, Takach N (2019a) Wellbore stability in naturally fractured formations featuring dual-porosity/single-permeability and finite radial fluid discharge. *J Petrol Sci Eng* 174:790–803
- Meng M, Zamanipour Z, Miska S, Yu M, Ozbayoglu EM (2019b) Dynamic stress distribution around the wellbore influenced by surge/swab pressure. *J Pet Sci Eng* 172:1077–1091. <https://doi.org/10.1016/j.petrol.2018.09.016>
- Mitchell RF (1988) Dynamic surge/swab pressure predictions. *SPE Drill Eng* 3:325–333. <https://doi.org/10.2118/16156-PA>
- Mme U, Pal S (2012) Effects of mud properties, hole size, drill string tripping speed and configurations on swab and surge pressure magnitude during drilling operations. *Inter J Pet Sci Technol* 5:143–153
- Rahimi R, Nygaard R (2015) Comparison of rock failure criteria in predicting borehole shear failure. *Int J Rock Mech Min Sci* 79:29–40. <https://doi.org/10.1016/j.ijrmmms.2015.08.006>
- Sadd MH (2009) *Elasticity: theory, applications, and numerics*. Academic Press, Burlington
- Schanz M (2009) *Poroelastodynamics: linear models, analytical solutions, and numerical methods*. *Appl Mech Rev* 62:030803. <https://doi.org/10.1115/1.3090831>
- Schuh FJ (1964) Computer makes surge-pressure calculations useful. *Oil Gas J* 31:96
- Tran MH, Abousleiman YN, Nguyen VX (2010) The effects of low-permeability mudcake on time-dependent wellbore failure analyses. In: IADC/SPE Asia Pacific drilling technology conference and exhibition. Society of Petroleum Engineers. <https://doi.org/10.2118/135893-MS>
- Ulusay R (2014) *The ISRM suggested methods for rock characterization, testing and monitoring: 2007–2014*. Springer, Berlin
- Wang HF (2000) *Theory of linear poroelasticity with applications to geomechanics and hydrogeology*. Princeton University Press, Princeton
- Wang Z, Miska S, Yu M, Takach N (2013) Effect of tripping velocity profiles on wellbore pressures and dynamic loading of drillstring. *AGH Drill Oil Gas* 30(1):269–286. <https://doi.org/10.7494/drill.2013.30.1.269>
- Wrana B, Pietrzak N (2013) Influence of inertia forces on soil settlement under harmonic loading. *Studia Geotechnica et Mechanica* 35:245–258. <https://doi.org/10.2478/sgem-2013-0019>
- Zamanipour Z (2015) *Automation of tripping operations in directional wellbores*. Master thesis, The University of Tulsa
- Zamanipour Z, Miska SZ, Hariharan PR (2016) Effect of transient surge pressure on stress distribution around directional wellbores. In: IADC/SPE drilling conference and exhibition. Society of Petroleum Engineers. <https://doi.org/10.2118/178831-MS>
- Zhang L (2008) A generalized three-dimensional Hoek–Brown strength criterion. *Rock Mech Rock Eng* 41:893–915. <https://doi.org/10.1007/s00603-008-0169-8>
- Zhang L, Zhu H (2007) Three-dimensional Hoek–Brown strength criterion for rocks. *J Geotech Geoenviron* 133:1128–1135. [https://doi.org/10.1061/\(ASCE\)1090-0241\(2007\)133:9\(1128\)](https://doi.org/10.1061/(ASCE)1090-0241(2007)133:9(1128))
- Zhang L, Cao P, Radha KC (2010) Evaluation of rock strength criteria for wellbore stability analysis. *Int J Rock Mech Min Sci* 47:1304–1316. <https://doi.org/10.1016/j.ijrmmms.2010.09.001>
- Zhang F, Kang Y, Wang Z, Miska S, Yu M, Zamanipour Z (2016) Real-time wellbore stability evaluation for deepwater drilling during tripping. In: SPE deepwater drilling and completions conference. Society of Petroleum Engineers. <https://doi.org/10.2118/180307-MS>
- Zhang F, Kang Y, Wang Z, Miska S, Yu M, Zamanipour Z (2018) Transient coupling of swab/surge pressure and in-situ stress for wellbore-stability evaluation during tripping. *SPE J* 23(4):1019–1038. <https://doi.org/10.2118/180307-PA>
- Zhao J (2000) Applicability of Mohr–Coulomb and Hoek–Brown strength criteria to the dynamic strength of brittle rock. *Int J Rock Mech Min Sci* 37:1115–1121. [https://doi.org/10.1016/S1365-1609\(00\)00049-6](https://doi.org/10.1016/S1365-1609(00)00049-6)
- Zhou Y, Zhao J (2011) *Advances in rock dynamics and applications*. CRC Press, Boca Raton
- Zienkiewicz OC, Chang CT, Bettess P (1980) Drained, undrained, consolidating and dynamic behavior assumptions in soils. *Geotechnique* 30:385–395. <https://doi.org/10.1680/geot.1980.30.4.385>
- Zoback MD (2010) *Reservoir geomechanics*. Cambridge University Press, Cambridge

Publisher's Note Springer Nature remains neutral with regard to jurisdictional claims in published maps and institutional affiliations.